Mesoscale modeling and satellite observation of transport and mixing of smoke and dust particles over northern sub-Saharan African region

Zhifeng Yang,[1] Jun Wang,[1] Charles Ichoku,[2] Edward Hyer,[3] and Jing Zeng[1]

Received 30 July 2013; revised 9 October 2013; accepted 13 October 2013; published 12 November 2013.

[1] The transport and vertical distribution of smoke and dust aerosols over the northern sub-Saharan African region are simulated in the Weather Research and Forecasting model with Chemistry (WRF-Chem), which uses hourly dynamic smoke emissions from the Fire Locating and Modeling of Burning Emissions database derived from the Moderate Resolution Imaging Spectroradiometer (MODIS) fire products. Model performance for February 2008 is evaluated using MODIS true color images, aerosol optical depth (AOD) measurements from the Aerosol Robotic Network, MODIS AOD retrievals, and the Cloud-Aerosol Lidar data with Orthogonal Polarization (CALIOP) atmospheric backscattering and extinction products. Specification of smoke injection height of 650 m in WRF-Chem yields aerosol vertical profiles that are most consistent with CALIOP observations of aerosol layer height. Between the equator and 10°N, Saharan dust is often mixed with smoke near the surface, and their transport patterns manifest the interplay of trade winds, subtropical highs, precipitation associated with the Intertropical Convergence Zone, and the high mountains located near the Great Rift Valley region. At the 700 hPa level and above, smoke layers spread farther to the north and south and are often above the dust layers over the Sahel region. In some cases, transported smoke can also be mixed with dust over the Saharan region. Statistically, 5% of the CALIOP valid measurements in February 2007–2011 show aerosol layers either above or between the clouds, reinforcing the importance of the aerosol vertical distribution for quantifying aerosol impact on climate in the Sahel region.

Citation: Yang, Z., J. Wang, C. Ichoku, E. Hyer, and J. Zeng (2013), Mesoscale modeling and satellite observation of transport and mixing of smoke and dust particles over northern sub-Saharan African region, *J. Geophys. Res. Atmos.*, *118*, 12,139–12,157, doi:10.1002/2013JD020644.

1. Introduction

[2] The northern sub-Saharan African (NSSA) region, extending from the equator to the lower fringes of the Sahara and stretching west to east from the Atlantic to the Indian Ocean coasts, plays a prominent role in atmospheric circulation, the birth of trans-Atlantic hurricanes, and the distribution of the Saharan mineral dust to other parts of the world [e.g., *Donnelly and Woodruff*, 2007; *Price et al.*, 2008; *Kaufman et al.*, 2005b]. This region is also subject to intense seasonal biomass burning and the transport of smoke and mineral dust particles from the Sahel region. Biomass burning in this region is mostly due to human activity and occurs primarily during the dry season from October to March every year. The regional vegetation is dominated by savannas and grasslands, with some woodlands and forests in the south. Thus, fires are much easier to ignite during the dry season. In terms of diurnal variability, fire activity peaks in the midafternoon and decreases to near insignificance at nighttime [*Ichoku et al.*, 2008; *Roberts and Wooster*, 2008]. The emission and transport of mineral dust particles in this region are more sporadic and occur in all seasons [e.g., *Greed et al.*, 2008; *Zhao et al.*, 2010; *Prasad et al.*, 2010; *Marey et al.*, 2011]. During the regional biomass burning (dry) season, the Intertropical Convergence Zone (ITCZ), which is an area of low pressure that forms where the Northeast Trade Winds (NETW) meet the Southeast Trade Winds (SETW) over the equatorial region, lies mainly to the south of the equator. The NETW can mobilize large amounts of mineral dust from the Bodélé depression and surrounding regions within the greater Lake Chad basin [e.g., *Ginoux et al.*, 2001; *Lau et al.*, 2009]. The mixture of mineral dust with smoke may significantly affect the health of the population as well as the direct and indirect radiative forcing in the region in complex ways. Furthermore, the interaction of these aerosols with clouds may also affect the downwind development of precipitation and circulation [*Kaufman et al.*, 2005a].

[1]Earth and Atmospheric Sciences, University of Nebraska—Lincoln, Lincoln, Nebraska, USA.
[2]Climate and Radiation Laboratory, NASA Goddard Space Flight Center, Greenbelt, Maryland, USA.
[3]Marine Meteorology Division, Naval Research Laboratory, Monterey, California, USA.

Corresponding author: J. Wang, Earth and Atmospheric Sciences, University of Nebraska—Lincoln, Lincoln, NE 68588, USA. (jwang7@unl.edu)

©2013. American Geophysical Union. All Rights Reserved.
2169-897X/13/10.1002/2013JD020644

[3] Although the Saharan mineral dust particles have been studied intensively in the past decade, much less attention is paid to smoke particles in the Sahel region and the mixing of Saharan mineral dust particles with smoke particles in both the horizontal and vertical dimensions. The distribution of fires in the Sahel region was first characterized from the Advanced Very High Resolution Radiometer (AVHRR) data in the 1990s [*Franca et al*., 1995; *Kaufman et al*., 1990]. Recent studies have examined satellite fire products to improve inventories for the entire African continent, including the development of geostationary fire detection products [*Roberts et al*., 2005; *Zhang et al*., 2012] and experiments combining the geostationary and polar-orbiting satellite data to derive the fire radiative power and energy that are indicators of fire intensity and emission [*Freeborn et al*., 2009, 2011; *Peterson and Wang*, 2013; *Peterson et al*., 2013]. The Dust And Biomass Experiment (DABEX) was conducted in early 2006 in Niamey, Niger, to study the characteristics and radiative effects of mineral dust and biomass burning aerosols emitted from the Sahara/Sahel regions using high-quality in situ measurements of their optical, physical, and chemical properties [*Capes et al*., 2008]. The DABEX study found a strong linear relationship between organic aerosol mass concentration and carbon monoxide concentration across the region [*Johnson et al*., 2008a, 2008b]. Also, based upon the SAharan Mineral dUst experiMent (SAMUM) conducted in January and February 2008, it was found that a dense desert mineral dust layer is dominant from the surface to 1500 m altitude, whereas a lofted layer of desert mineral dust mixed with biomass burning smoke can be found from 1500 to 5000 m [*Tesche et al*., 2009]. Furthermore, using data from SAMUM, *Haywood et al*. [2008] showed the importance of the interaction between the organic carbon and mineral dust aerosol, which can cause a constant ratio of excess carbon monoxide to organic carbon to be maintained. They also summarized that meteorological models should include the effects of both mineral dust and biomass burning aerosol on the radiation budget for accurate weather forecasts and climate simulations [*Haywood et al*., 2008].

[4] This study focuses on smoke and mineral dust transport mechanisms over the NSSA region, with emphasis on understanding the distribution patterns of smoke and mineral dust in the vertical dimension. Reliable simulations of mineral dust and smoke vertical profiles are important to understanding their respective radiative feedback to clouds and climate [*Haywood et al*., 2008]. Both global and regional climate models were employed in the past to study smoke radiative effects at monthly to seasonal scales over the Sahel region [*Myhre et al*., 2003a, 2003b; *Malavelle et al*., 2011]. While those studies showed the significance of the smoke particles on the regional climate, the diurnal variation of smoke emission and smoke injection height, two key factors that regulate the aerosol vertical profile [*Wang et al*., 2006], was not observationally constrained in those models. The monthly time step used in previous studies is insufficient to model the distinct contrast of burning activities between day and night, as well as short-term regional variation in burning; and the evaluation of those model results relied on ground-based (Aerosol Robotic Network (AERONET)) and passive satellite (Moderate Resolution Imaging Spectroradiometer (MODIS), Multiangle Imaging Spectroradiometer, Ozone Monitoring Instrument) remote-sensing products that lack the necessary information on the aerosol vertical profile.

[5] This study is designed to use a mesoscale model and satellite observations to understand the smoke and mineral dust transport processes over the NSSA region, especially their mixing in the vertical direction. The Weather Research and Forecasting model with Chemistry (WRF-Chem) is used, and smoke emission is specified from the Fire Locating and Modeling of Burning Emissions (FLAMBE) database derived from MODIS fire products. Model performance is evaluated in the horizontal using MODIS true color images, ground-based measurements of Aerosol Optical Depth (AOD) from AERONET, and MODIS retrievals, and in the vertical using the Cloud-Aerosol Lidar and Infrared Pathfinder Satellite Observations (CALIPSO) Cloud-Aerosol Lidar with Orthogonal Polarization (CALIOP) atmospheric backscattering and extinction products. The time period of focus for this study is February 2008. This study differs from past studies in that (1) a mesoscale chemistry transport model WRF-Chem is used together with hourly fire emission to study the temporal evolution of smoke transport pathways during the transition from dry season (October to March) to wet season (April to September), (2) CALIOP observations are used to constrain the smoke injection height in WRF-Chem as well as to evaluate the WRF-Chem simulation, (3) both smoke and mineral dust transports and their vertical mixing are considered together in three dimensions, and (4) statistics are analyzed on the relative positioning of smoke and cloud layers in the vertical dimension. We describe the data in section 2, the method in section 3, and the result and analysis in section 4, and we conclude the paper in section 5.

2. Data Sets and Study Area

[6] The area of interest for this study is the NSSA region (Figure 1b). Important data used in this study include the following: (1) hourly smoke emissions from FLAMBE database, (2) MODIS Dark Target (DT) and Deep Blue (DB) AOD at 550 nm wavelength, (3) AERONET AOD at 550 nm, (4) CALIOP lidar observations including its Level 1 and 2 products, and (5) meteorological data from National Center for Environmental Prediction (NCEP) Global Final Analysis (FNL).

2.1. FLAMBE Emission

[7] The smoke aerosol emissions used in this study are from the FLAMBE inventory, which is estimated using the method originally proposed by *Seiler and Crutzen* [1980] [*Reid et al*., 2004; *Reid et al*., 2009]. FLAMBE emission uses fire detection products from geostationary and polar-orbiting (Terra and Aqua MODIS) satellites. These fire products (e.g., MODIS Collection 5; [*Giglio et al*., 2003]) include the location and time of the fire. The emission of smoke particles is estimated as a function of the amount of fuel mass available for combustion, the average mass fraction of carbon in the fuel, the combustion factor, the total area burned, and the emission factor [*Reid et al*., 2009].

[8] Currently, FLAMBE uses MODIS fire products to estimate the smoke emission over the NSSA region. While MODIS/Terra and MODIS/Aqua can detect fires three to four times per day that is sufficient to contrast between high fire activity during the day and low activity during the night,

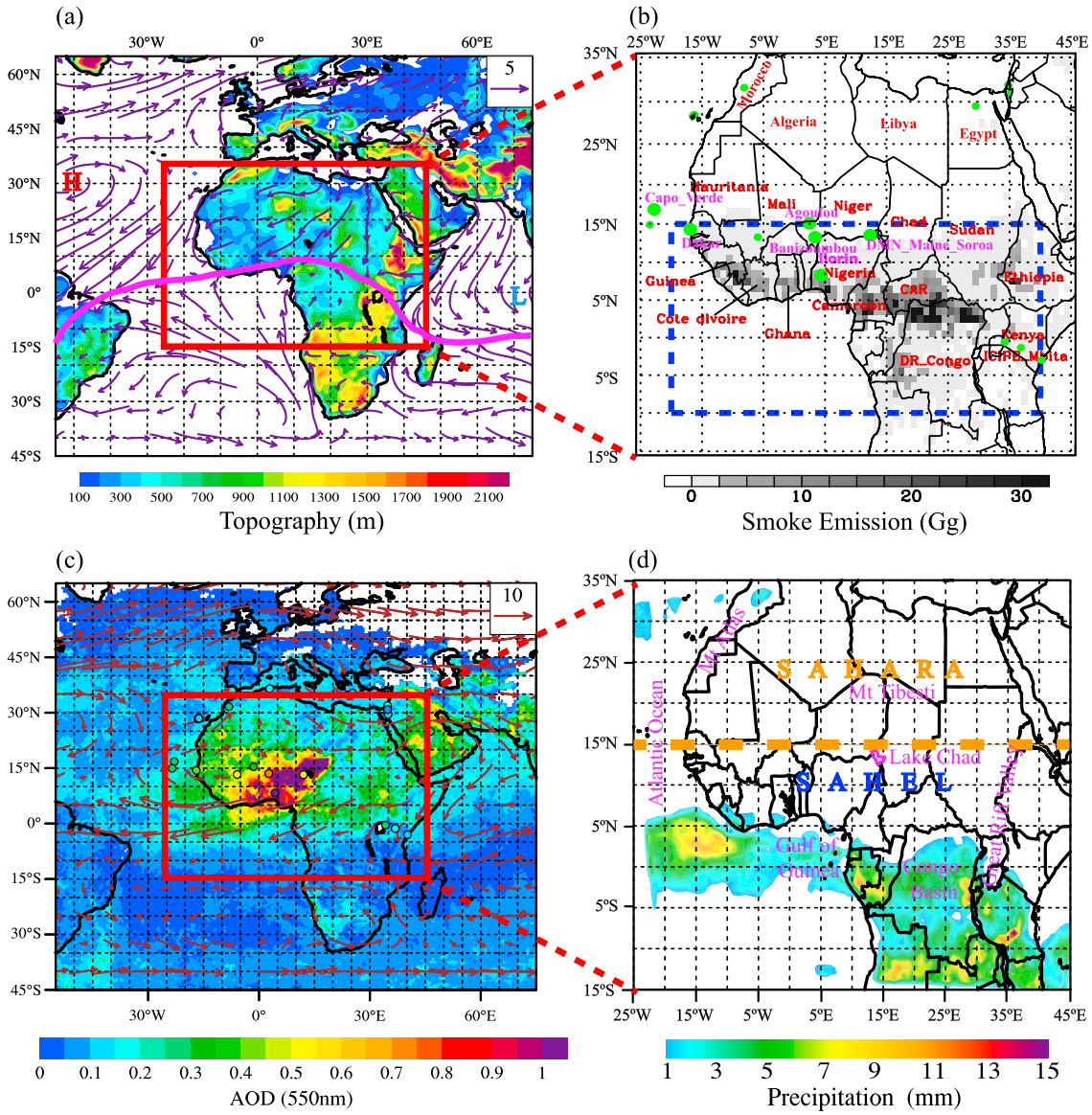

Figure 1. (a) WRF-Chem topography height and NCEP/National Center for Atmospheric Research (NCAR) reanalysis monthly averaged surface flow patterns, including high-pressure system (red "H"), low-pressure system (blue "L"), and ITCZ (pink curve). The red square corresponds to the study region (Figure 1b). (b) WRF-Chem coarse-grid domain and fine-grid domain (blue dashed square) overlaid with the map of gray-colored total smoke emissions (1 Gg = 10^9 g) from FLAMBE database during February 2008. AERONET sites are represented in green dots, and the names of relevant countries are labeled in red color. The relative bigger green dots, coupled with pink-colored names, are selected for analysis in this study. (c) MODIS AOD (550 nm) monthly average in February 2008 overlaid with monthly averaged 700 hPa flow patterns and AERONET monthly averaged AOD (500 nm, color-coded dots with black circle). (d) WRF-Chem-simulated monthly averaged 24 h precipitation in February 2008, superimposed with landform names [NCL, 2013].

a climatology of fire diurnal cycle is needed to distribute the smoke emissions between MODIS overpass times. The assumptions made in this study include the following: (1) fires have a duration of 24 h from the hour of first detection, and roughly 90% of smoke emissions are released during daylight hours, and (2) fire area is assumed as 62.5 ha for each fire pixel that MODIS detects [*Reid et al.*, 2009; *Wang et al.*, 2013]. Past studies show that FLAMBE underestimates smoke emissions in different regions by a factor of 1.5–3 [*Reid et al.*, 2004, 2009; *Wang et al.*, 2006]. Based on preliminary model testing (not shown in this paper), FLAMBE smoke emission values are multiplied by a scale factor of 1.8 in this study before they are applied in WRF-Chem. This scale factor is based on the scale factor value of 1.5 provided by *Reid et al.* [2009] for this region as adjusted for the current study using observations from both MODIS and AERONET.

[9] During 1 to 29 February 2008, a large number of fire events were observed from satellite across the NSSA, particularly between 10°N and the equator (Figure 1b), producing

an estimated 2.96 Tg smoke emission (total particulate matter) in total. Most of the smoke emissions are distributed over Guinea and Cote d'Ivoire (Region A), Ghana and Nigeria (Region B), and the central part of Africa (Region C) including the Cameroon, Central African Republic, Congo, and Democratic Republic of the Congo (DR Congo). Significant amounts of smoke are present over the west of DR Congo due to lack of precipitation in this region during this dry season.

2.2. MODIS AOD

[10] The MODIS instruments aboard Terra (launched in December 1999) and Aqua (launched in May 2002) satellites measure spectral radiance in 36 channels, with resolutions ranging from 250 m to 1 km at nadir. Each MODIS views a swath of 2300 km from about 705 km above the Earth in a polar orbit and covers the whole Earth's surface every 1 to 2 days. Three of the 36 channels (470 nm, 660 nm, and 2130 nm) are used to retrieve standard AOD, which is then interpolated in the midvisible spectrum (550 nm), whereas over ocean, AOD retrieval is performed at seven wavelengths (470 nm, 550 nm, 660 nm, 870 nm, 1240 nm, 1630 nm, and 2130 nm). Other aerosol parameters available from MODIS include fine aerosol fraction and Angstrom exponent. MODIS aerosol products up to the current version (Collection 5) are provided at a resolution of 10 km. AOD is reported to have an uncertainty of $\pm(0.05 + 0.15\tau)$ over dark land and $\pm(0.04 + 0.10\tau)$ over ocean, where τ is the MODIS retrieved AOD [*Kaufman et al.*, 1997; *Levy et al.*, 2007; *Levy et al.*, 2010; *Remer et al.*, 2005]. An AOD retrieval algorithm over bright surfaces (e.g., Sahara desert) called "Deep Blue" is also available, with an uncertainty of 20%–30% based on comparison with AERONET Sun photometer observations [*Hsu et al.*, 2006]. This uncertainty can be improved to 18% around North Africa using empirical corrections and quality assurance procedures [*Shi et al.*, 2013]. Therefore, in this study, the retrieved standard ("Dark Target") AOD (550 nm) and "Deep Blue" AOD (550 nm) are used over land, and standard AOD (550 nm) is applied over ocean. The MODIS aerosol Level 2 Collection 5 products (MOD_04 and MYD_04 from Terra and Aqua, respectively) were selected to compare with model simulations of AOD for smoke and mineral dust particles.

2.3. AERONET

[11] AERONET comprises a network of ~400 ground-based Sun-sky scanning radiometer systems (or Sun photometers), located at important observation sites around the world and providing retrievals of precipitable water, as well as aerosol optical properties, such as AOD at various wavelengths (e.g., 340 nm, 380 nm, 440 nm, 500 nm, 675 nm, 870 nm, and 1020 nm), Angström exponent, aerosol refractive index, size distribution, and fine-mode fraction [*Holben et al.*, 1998; *Dubovik et al.*, 2000]. Three AERONET data quality levels are available: Level 1.0 (unscreened), Level 1.5 (cloud screened), and Level 2.0 (cloud screened and quality assured). The uncertainty in Level 1.5 AOD data is estimated to be in the range $0.01 \sim 0.05$ (air mass = 1) [*Eck et al.*, 1999; *Smirnov et al.*, 2000]. For the quality-assured Level 2.0 data used in this study, the uncertainty of AOD measurements is about ±0.01 [*Holben et al.*, 2001]. For comparison with model simulations in this study, the AERONET-measured AODs at 675 nm and 440 nm are used to interpolate the AOD at 550 nm (using the AERONET Angström exponent). A total of 21 sites with Level 1.5 and Level 2.0 data were available in the study region during February 2008. Considering the dominant spatial influences of smoke and mineral dust, six sites were selected as relevant for this study, namely, DMN_Maine_Soroa (13.2° N, 12.0°E), Banizoumbou (13.5°N, 2.7°E), Agoufou (15.3° N, 1.5°W), Dakar (14.4°N, 16.9°E), Capo_Verde (16.7°N, 22.9°W), and Ilorin (8.3°N, 4.3°E). Site names from the AERONET database are used in this paper. These have a close but not exact geographic and orthographic correspondence with the instrument locations—full details are available at http://aeronet.gsfc.nasa.gov/. These sites are shown as large green dots, with site names shown in pink in Figure 1b. The selection of these sites considers the availability of Level 2.0 (Ilorin) and Level 1.5 (when Level 2.0 is not available, e.g., at DMN_Maine_Soroa, Banizoumbou, Agoufou, Dakar, and Capo_Verde) data and the opportunity to observe both the dust and smoke aerosols (section 4.2).

2.4. CALIOP

[12] CALIOP is a two-wavelength polarization active lidar aboard the CALIPSO satellite, launched in April 2006 [*Winker et al.*, 2009]. CALIOP performs global profiling of aerosols and clouds in the troposphere and lower stratosphere. The data used in this study include CALIOP lidar Level 1B products and Level 2 cloud and aerosol profile products, which can be downloaded from https://eosweb.larc.nasa.gov/project/calipso/calipso_table. Level 1B data are half orbit (night and day) geolocated, calibrated lidar profiles, and viewing geometry products; it has different altitude ranges (−2.0 km to −0.5 km, −0.5 km to 8.3 km, 8.3 km to 20.2 km, 20.2 km to 30.1 km, and 30.1 km to 40.0 km), with different horizontal resolutions of 1/3 km, 1/3 km, 1 km, 5/3 km, and 5 km and vertical resolutions of 300 m, 30 m, 60 m, 180 m, and 300 m, respectively. CALIOP Level 2 products have a horizontal resolution of 5 km and a vertical resolution of 60 m up to 20 km.

[13] CALIOP Level 2 processing involves first separating the aerosol and cloud layers based on an algorithm developed by *Liu et al.* [2004, 2009], then determining the aerosol type and cloud ice-water phase, and finally retrieving the profiles of particle backscatter and extinction coefficients using a hybrid extinction retrieval algorithm [*Liu et al.*, 2004, 2009; *Winker et al.*, 2009]. Considering the realistic altitude range of aerosol vertical distribution, only data under 20 km height were selected for this study. CALIOP-attenuated backscatter profiles at 532 nm from Level 1B products, extinction coefficient and particulate depolarization ratio profiles at 532 nm, and vertical feature mask from Level 2 products were selected to evaluate WRF-Chem vertical profile simulations.

2.5. Meteorological Data

[14] The meteorological data used in this study were the NCEP Global Final Analyses (FNL) data, which are available for the period of 1999–present [*Kalnay et al.*, 1996; *Kistler et al.*, 2001]. The NCEP FNL data are reported every 6 h at a spatial resolution of 1° globally, with 26 vertical levels from 1000 to 10 hPa (excluding the surface). These data are available from http://rda.ucar.edu/datasets/ds083.2/. The NCEP FNL data were used to specify the meteorological initial and boundary conditions in the WRF-Chem simulations.

Table 1. Configuration Options Employed by WRF-Chem in This Study

Atmospheric Processes	Model Option
Microphysics	WSM5
Cumulus	Grell
Land Surface Model	Noah
Boundary Layer Scheme	YSU
Shortwave radiation	Goddard
Longwave radiation	RRTM
Gas-phase mechanism	RADM2
Aerosol model	MADE/SORGAM
Dust Scheme	GOCART

3. Model Description

3.1. WRF-Chem and Assimilation of FLAMBE Emission

[15] WRF-Chem is the Weather Research and Forecasting (WRF) model coupled "online" with a chemistry package, including aerosol life cycle, aerosol-cloud-radiation interactions, and gas-phase chemistry [*Fast et al.*, 2006]. WRF is a fully compressible and nonhydrostatic model (with a runtime hydrostatic option). Its vertical coordinate is a terrain-following hydrostatic pressure coordinate. WRF-Chem has all the capabilities of WRF, and the meteorological and chemical components can be predicted simultaneously. More detailed information can be found in the works of *Grell et al.* [2005] and *Fast et al.* [2006]. WRF-Chem version 3.3.1 has been applied over the NSSA region for this study.

[16] The specification of smoke emission rate in WRF-Chem follows the work of *Wang et al.* [2006, 2013]. The smoke emission rate within a grid cell of area A (m^2) is calculated as

$$\left(\frac{\partial C}{\partial t}\right)_{emission} = \frac{\sum_j F_j}{A \cdot H \cdot \Delta t},$$

where j represents the jth fire within that grid, F is the smoke emission (kg), H is the injection height (m), and the smoke particles are well mixed in all model layers below this height. Since hourly smoke emission is used, Δt is set to 1 h.

3.2. Model Configuration

[17] The main model options for the physical and chemical schemes used in this study are listed in Table 1. The microphysics and cumulus parameterization used here are, respectively, the WRF single-moment five-class (WSM5) [*Hong et al.*, 2004] scheme and the Grell ensemble cumulus scheme [*Grell and Devenyi*, 2002]. The land surface model is the Noah Land Surface Model [*Chen and Dudhia*, 2001]. The boundary layer scheme is the Yonsei University (YSU) scheme [*Hong et al.*, 2006]. The shortwave radiation scheme is the two-stream multiband Goddard model [*Chou et al.*, 1998]. The longwave radiation scheme is the Rapid Radiative Transfer Model (RRTM) [*Mlawer et al.*, 1997]. The simulation of aerosol processes is based on the Regional Acid Deposition Model, version2 (RADM2) photochemical mechanism [*Stockwell et al.*, 1990]. The aerosol modules are the Modal Aerosol Dynamics Model for Europe (MADE) [*Ackermann et al.*, 1998] and the Secondary Organic Aerosol Model (SORGAM) [*Schell et al.*, 2001]. The mineral dust emission scheme used is that of the Goddard Global Ozone Chemistry Aerosol Radiation and Transport (GOCART) model [*Ginoux et al.*, 2001]. GOCART is coupled with MADE/SORGAM for mineral dust simulation. The mineral dust source function of GOCART over North Africa is shown in Figure 2 [*Zhao et al.*, 2010].

[18] The WRF-Chem simulation in this study was conducted for the period of 15 January to 29 February 2008. The output is compared with observations during 1–29 February, with the first 15 days of simulation used as spin-up. An outer nest with a resolution of 81 km and 27 vertical levels (from 1000 hPa to 10 hPa) over an extended domain (35.0°N–15.0°S, 25.0°W–45.0°E) gives a large-scale synoptic view of the NSSA region. The 27 km nest domain (same vertical levels as in the outer nest) focuses on the fire emission source region (15.0°N–10.0°S, 20.0°W–40.0°E), as delimited in Figure 1b with a blue dashed square. Since the purpose of this study is to characterize smoke and mineral dust transport, the (local) background aerosol and long-range transport from other sources, as well as radiative feedback between aerosol particles and meteorology, were ignored [*Wang et al.*, 2013]. All the smoke emissions are treated as particulate matter less than 2.5 µm aerodynamic diameter ($PM_{2.5}$) emission in the model. In order to study the influence of injection height on smoke transport, three sensitivity experiments were conducted with three different injection heights: 500 m, 650 m, and 2 km, as will be discussed in the results section below.

4. Results and Analysis

4.1. Overview

[19] The African continent is surrounded by the Atlantic Ocean to the west, Indian Ocean to the southeast, Red Sea

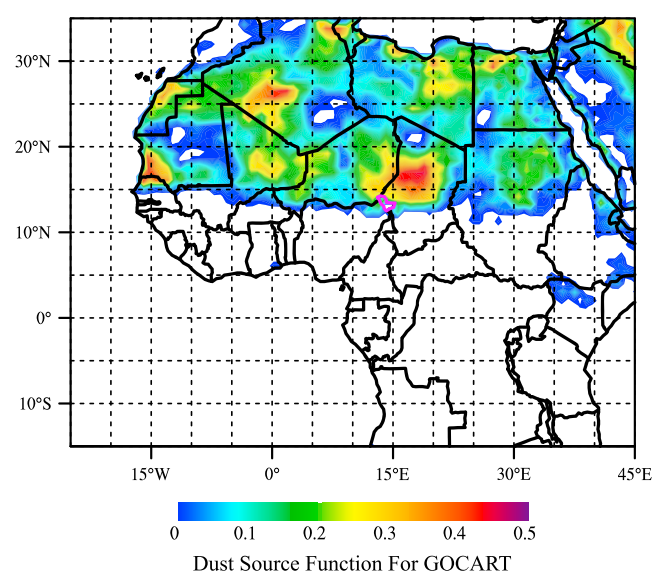

Figure 2. Dust source function (S) for GOCART from WRF-Chem. Lake Chad is marked with a pink curve. The dust source function is the fraction of alluvium available for wind erosion. For each grid cell with mean elevation of z, $S = \left(\frac{z_{max} - z_i}{z_{max} - z_{min}}\right)^5$, where S is the probability to have accumulated sediments, z_{max} and z_{min} are the maximum and minimum elevations in the surrounding 10° × 10° topography, respectively [*Ginoux et al.*, 2001].

to the northeast, and the Mediterranean Sea to the north. Typically, the Sahara desert and Sahel region are divided by the north-south precipitation gradient of 1 mm yr^{-1} km^{-1} which extends for over 6000 km between 15°N and 17°N, from the Atlantic Ocean to the Red Sea [*Tucker and Nicholson*, 1999]. Most of the Sahel region is flat with an average topographic height of ~500 m above mean sea level, whereas in West Africa, the topographic height is lower than 300 m (Figure 1a). However, several mountains as high as 2000 m are also situated near the Great Rift Valley area in East Africa, including Mount Turkana (centered at 10°N, 40°E), Mount Kenya (0°, 35°E), and Mount Rwenzori (3°S, 30°E), which, as will be shown in section 4.3, block the eastward transport of the Sahel smoke as well as dust from the Bodélé Depression. The Hoggar and Tibesti Plateaux to the north of Lake Chad affect the spread of smoke and mineral dust toward the north. The Atlas Mountains located northwest of Sahara desert influence smoke propagation to the northwest. The main mineral dust sources are primarily situated in south central Chad, southwest of Algeria, and south of Mauritania (Figure 2; based upon *Ginoux et al*., 2001).

[20] In response to the topography and general atmospheric circulation, the key synoptic systems in our study region (Figure 1b) include the following: (a) the Intertropical Convergence Zone (ITCZ), shown in Figure 1a as the pink curve over the monthly average of the surface wind, which is manifested as northeasterly wind over the Sahara desert and prevailing southeasterly wind over the Gulf of Guinea, southwest of the Sahel region; (b) the Azores High, the strong high-pressure system, which is centered around 30°N and 40°W over the subtropical Atlantic Ocean northwest of the ITCZ, resulting in the northeasterly winds that in turn can transport the Sahara mineral dust to west Atlantic and sometimes even the Amazon forest; and (c) the low-pressure system that is located southeast of the Sahel region and centered around 55°E on the equator, leading to the formation of precipitation over this region. It is noted that during February, the ITCZ often moves from the north of the equator over the continent and slowly rolls south of the equator over the Atlantic Ocean and Indian Ocean. Precipitation and convergence of water vapor usually occur over the southern part of the surface confluence zone (Figure 1d), suggesting a southward-tilt structure of the convection. The precipitation areas are mainly situated south of the equator over the African continent and west of the Gulf of Guinea, whereas less precipitation occurs south of the Gulf of Guinea and southeast of the study region. The annual precipitation over the Sahara desert is less than 1 mm.

[21] Transports of smoke and mineral dust often result in high AOD over the NSSA region. In February 2008, monthly averages of MODIS and AERONET AODs at 550 nm were as large as 1.0 near Nigeria, Ghana, and the northern rim of the Gulf of Guinea. Low AODs (Figure 1c) are associated with high precipitation. The AOD distribution can be further explained by the flow patterns at the 700 hPa layer that are significantly different from the surface ones. The trade winds north of the equator are shifted southward and become stronger (as compared to their surface counterparts), resulting in high AOD northwest of the Gulf of Guinea at 700 hPa. Meanwhile, over the Sahara desert region, westerly wind dominates and provides conditions that are favorable for transporting aerosols to and rendering high AOD over Nigeria.

4.2. Smoke and Mineral Dust Events

[22] The air over the NSSA region is mainly polluted by both mineral dust from the Sahara desert and smoke emitted by savanna fires in the Sahel region. AERONET observations in the study area recorded several pollution events that occurred during February 2008. The locations of the available AERONET sites in February 2008 are mainly near the southern border of the Sahara desert (north of the smoke emission source region; Figure 1b). Therefore, most of the AERONET sites can only be indicative of mineral dust transport to the Sahel region from the Sahara desert (Figures 3a, 3c, and 3e), except for Ilorin in Nigeria (as shown in the inset of Figure 3g), which is downwind of the smoke emission area and thus can characterize the temporal variation of both mineral dust and smoke. Dakar and Capo_Verde are, respectively, at the west coast and off the coast of western Africa (Figures 3i and 3k) and sometimes can capture the transported mixture of smoke and mineral dust particles.

[23] The timing of polluted events can be studied by analyzing the time series of measured total and coarse-mode AOD, as well as the WRF-Chem-simulated smoke and mineral dust mass loadings at different AERONET sites (Figure 3). The timing of smoke and mineral dust events, during which total AODs at various stations are more than the corresponding monthly averages (dashed lines in Figures 3a, 3c, 3e, 3g, 3i, and 3k), varies at different AERONET sites (as marked with color-coded shadows in Figure 3), reflecting the trajectory of aerosol transport. The DMN_Maine_Soroa site is the one closest to the mineral dust source region (Figure 3a). Four mineral dust events occurred at this site during 2–3, 14–15, 19–20, and 25–27 February, with correspondingly higher coarse-mode AOD (Figure 1b). Banizoumbou and Agoufou are downwind sites, which have similar timings of mineral dust events as DMN_Maine_Soroa, except that there is a 1–2 day delay (Figures 3c and 3e). The aforementioned three sites can be considered as representative of mineral dust and can be used to evaluate the timing of dust events simulated in WRF-Chem. In contrast, the Ilorin site, as will be discussed below, has three events with dust and smoke mixtures during 1–4, 15–18, and 20–23 February (Figure 3g), each corresponding to moderate coarse-mode AOD. Dakar and Capo_Verde show the major polluted events during 17–24 February where smoke and mineral dust particles are mixed, resulting in less coarse-mode AODs observed. The Ilorin, Dakar, and Capo_Verde sites can be used to evaluate model-simulated timing of dust and smoke-mixed events.

[24] Smoke events can also be inferred from the temporal variations of MODIS fire pixel counts (Figure 4). The fire counts represent both daytime (Figure 4, red curve) and nighttime (Figure 4, blue curve) fires detected by MODIS. The monthly average of the daytime- and nighttime-detected fire counts in the NSSA region are around 4300 and 130, respectively, indicating that most of the fires occur during the daytime. Big fire events can be distinguished from the time series variations. Four big fire events are detected during 1–4, 13–15, 18–19, and 21–23 February, which is consistent with the observed high AOD values and moderate fraction of coarse-mode AOD in Ilorin, Dakar, and Capo_Verde sites. Apparently, smoke and dust transport occurred the same days

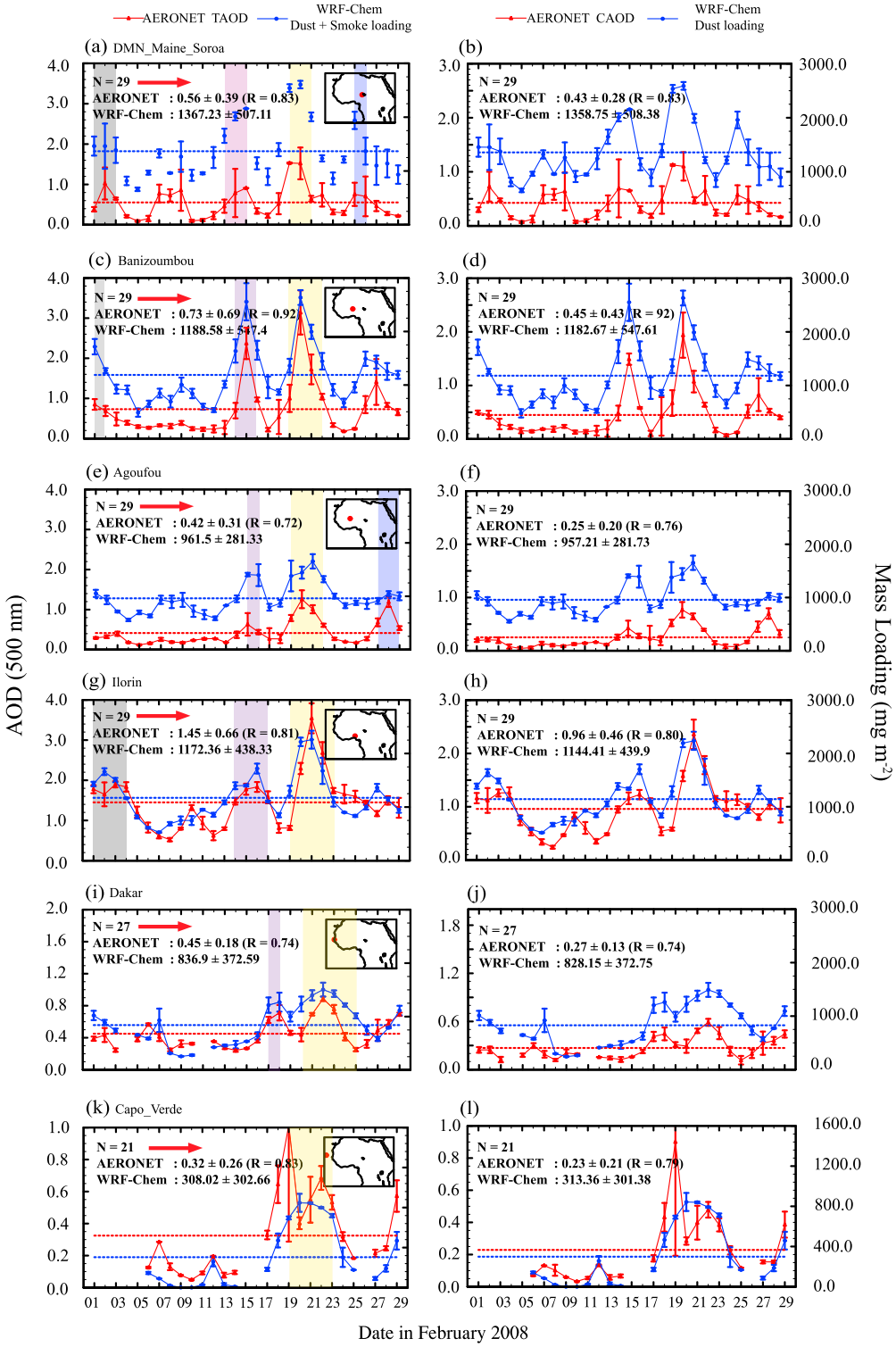

Figure 3. (left column) Time series of daily averaged AERONET observed total AOD (TAOD, 500 nm, red line) and WRF-Chem-simulated mineral dust and smoke mass loading (mg m^{-2}, blue line) at various AERONET ground-based sites during February 2008. Also shown are the monthly averaged AOD for AERONET (red dashed line) and mass loading for WRF-Chem (blue dashed line). The inset map on the upper right of each panel shows the location of the site (denoted as red dot). (right column) Similar to the left column but for AERONET coarse-mode AOD (CMAOD, 500 nm) and dust mass loading for WRF-Chem. Each row is for the same AERONET site. Also shown in each panel are the number of comparison pairs (N), monthly mean ± standard deviation for both AERONET and WRF-Chem, and the correlation coefficient (R) between AERONET and WRF-Chem.

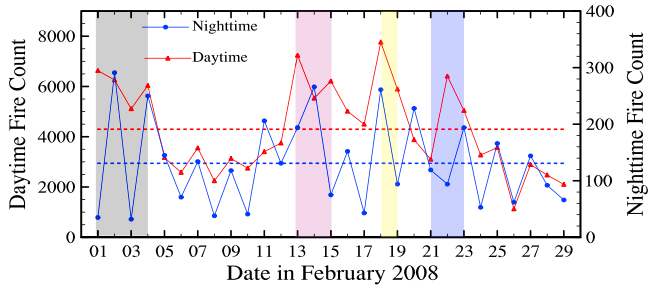

Figure 4. Time series of MODIS (Aqua) detected daytime (red solid line with triangle marker) and nighttime (blue solid line with solid circle) fire counts in the study region during February 2008. The horizontal line shows the monthly averaged fire counts.

on several occasions, including 2–3, 7–9, 14–15, and 19–20 February 2008.

[25] The daily averaged observed AOD and modeled mass loadings have similar trends and high-correlation coefficients. The correlation coefficient between total AOD from AERONET and the sum of mineral dust and smoke mass loadings from WRF-Chem is 0.83 (Figure 3a). Coarse-mode dust is dominant near the dust source region, with large observed coarse-mode AOD and modeled mineral dust mass loadings (Figure 3b). The correlation coefficient between observed coarse-mode AOD and modeled mineral dust mass loading is 0.83 for DMN_Maine_Soroa, suggesting the reliability in WRF-Chem-simulated timing of dust events.

[26] Dust is blown further to the west, with the impact of the westward flow patterns indicated near the mineral dust source region (Figures 1a and 1c). The evolution of mineral dust transport is evident at two AERONET sites, Banizoumbou and Agoufou (Figures 3c–3f), where WRF-Chem also captured the time variation of mineral dust and smoke mass loadings as characterized by the observed high AOD ($R = 0.9$ in Figures 3c and 3d and ~0.7 in Figures 3e and 3f). However, regional dust particles can accumulate during transport, resulting in higher AODs downwind compared to the dust source region. This is especially true of the mineral dust events that occurred on 14–16, 19–22, and 26–28 February. The monthly averages of total AODs and coarse-mode AODs have increased from 0.56 to 0.43, respectively, at the source region (DMN_Maine_Soroa) to 0.73 and 0.45, respectively, at the Banizoumbou and Agoufou sites. The correlations between WRF-Chem and AERONET AOD in DMN_Maine_Soroa and Agoufou are not as good as others. One possible reason is that the aerosols around these two sites are not only affected by smoke and dust but also affected by the local sources from the industrial and residential emissions that are not considered in our simulation.

[27] The other three AERONET sites can be used to study the timing of smoke and mineral dust mixing. Ilorin is positioned at the northern boundary of the Guinea savannah zone and under the influences of the annually alternating southward and northward passages of the ITCZ. When the ITCZ appears slightly south of Ilorin, the prevailing northeasterly wind, known as the "Harmattan," brings in air containing Saharan dust. The dust plumes originate from the Bodélé Depression in the Chad Basin. This is a climatically important region due to its location in a desert transition zone and because of the influence of the dusty Harmattan wind, which is persistent for prolonged periods of time and characterized by steady dusty conditions with high aerosol loading. Based upon the timing of the pollution events at Ilorin (Figure 3g) and the analysis discussed in the last two paragraphs, it can be inferred that the first event in Ilorin on 1–4 February was caused by smoke, the second event on 14–18 February resulted from the mixture of smoke and mineral dust, and the third event on 20–23 February was the consequence of a dust event.

[28] Finally, the coastal site of Dakar and island site of Capo_Verde are further away from both the dust and smoke source regions, and their AOD time series show that the aerosol loading during the mineral dust and smoke events is much lower, reflecting the effectiveness of atmospheric dispersion of aerosols with the prevailing easterly trade winds. Compared to the monthly averaged observed AOD of 0.5 and modeled mass loading of 600 mg/m^2 in the mineral dust and smoke source region, the values of these parameters are 0.3 and 200 mg/m^2, respectively, over the leeward regions (Figures 3i and 3k), due to deposition while in transport. Overall, the WRF-Chem simulation captured the timing of the mineral dust and smoke events during 17–24 February, except 19 February, on which day AERONET observation has much higher AOD. This higher value may have been caused by local pollution.

4.3. Smoke and Mineral Dust Transport Pathway

[29] Specific smoke and mineral dust events are extracted out for further exploration. The events on 3, 15, 21, and 27 February 2008 are selected as case studies, with 3 and 15 February representing coupled mineral dust and smoke events, whereas 21 and 27 February represent mineral dust events with little smoke influence.

[30] Fire occurrence during the daytime is much higher than during the nighttime (Figure 4), with the average MODIS daily fire count for the study region being about 4300 and 130 for daytime and nighttime overpasses, respectively. This is because these fires are often ignited by farmers as part of their routine agricultural practices that primarily occur during the daytime [*Wang et al.*, 2006]. Because of the limitations of satellite orbits, higher fire sensitivity within MODIS swath is at nadir rather than at the limb [*Freeborn et al.*, 2011; *Hyer et al.*, 2013]. MODIS daytime (red dots) and nighttime (green dots) fire detections are plotted over MODIS true color images in Figures 5a–5d, which show that fires are mainly located along the Sahel region, between the equator and 15°N. However, the fire count cannot represent the smoke density completely. *Ichoku et al.* [2008] showed that one daytime satellite overpass cannot fully capture all the fire, as fire counts can vary significantly both spatially and temporally between satellite overpasses. This is why smoke density can be high even when fire counts appear low. Between the beginning and end of the February, the main precipitation belt associated with the ITCZ over the African continent moves from south of the equator (~5°S) during that first smoke event to north of the equator (~5°N) during the last smoke event (Figure 5, last row).

[31] On 3 February 2008, AODs larger than 0.5 are limited to between the equator and 15°N and appear to be concentrated in two areas: north of the Gulf of Guinea (centered at 8°N, 0°E) and north of the Congo Basin (centered at 0°N,

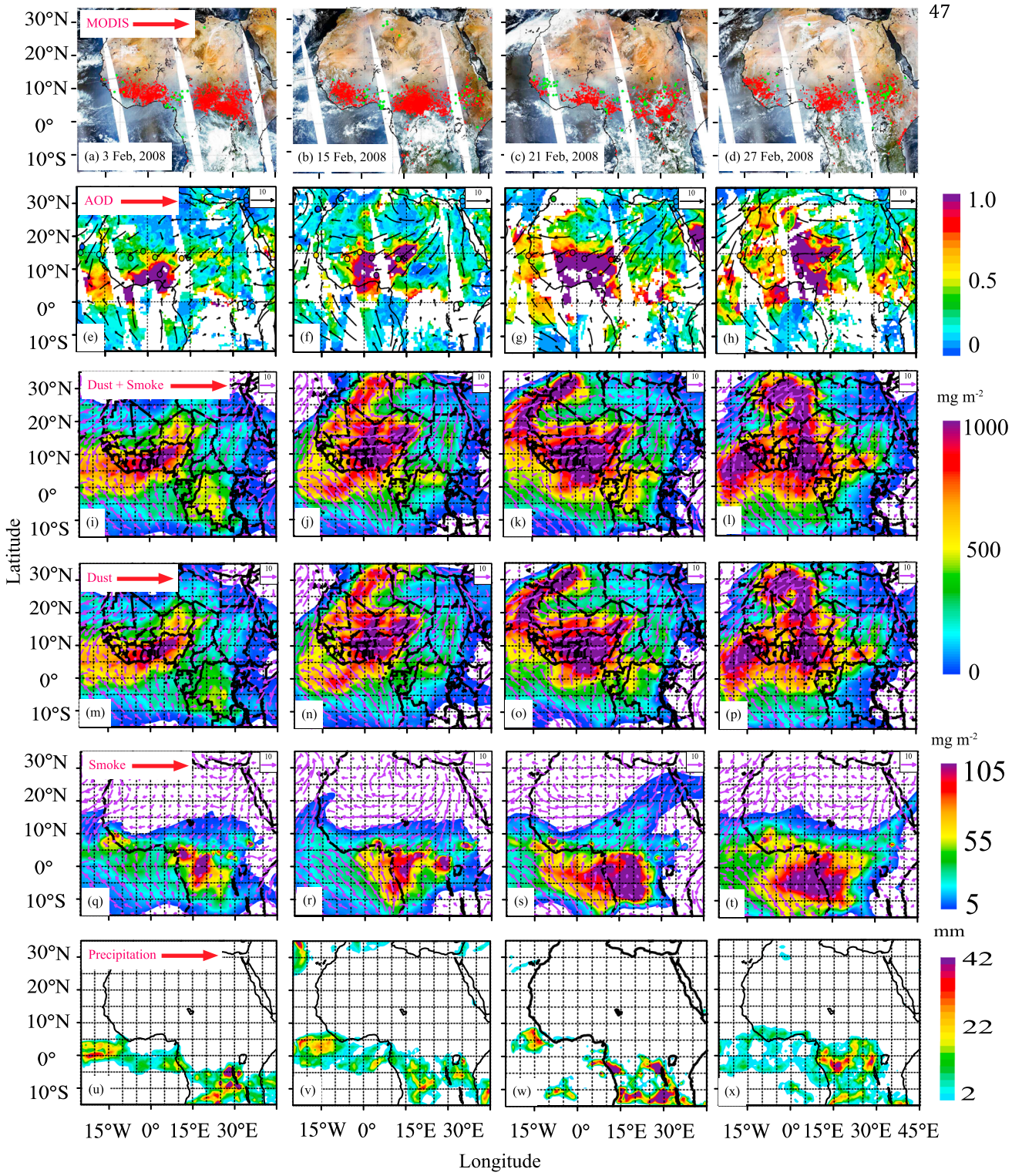

Figure 5. (a–d) MODIS three-band color overlay images (band 1—red, band 4—green, and band 3—blue) from Aqua satellite on 3, 15, 21, and 27 February 2008, respectively. Red and green dots indicate the location of daytime and nighttime fires detected by MODIS, respectively. Note that the fire dot scale has been enlarged in order to portray the fires more clearly in the figure. (e–h) MODIS AOD (550 nm) overlaid with NCEP/NCAR reanalysis of daily averaged surface wind vector and AERONET daily averaged AOD (500 nm). (i–l) Modeled daily-averaged mass loading (mg m^{-2}) of dust and smoke particles on the days corresponding to the ones in Figures 5a–5d, respectively; also overlaid is the simulated wind speed near the surface. (m–p) Same as Figures 5i–5l but for modeled dust mass loading. (q–t) Same as Figures 5i–5l but for modeled smoke mass loading. (u–x) Same as Figures 5i–5l but for the simulated 24 h accumulated precipitation.

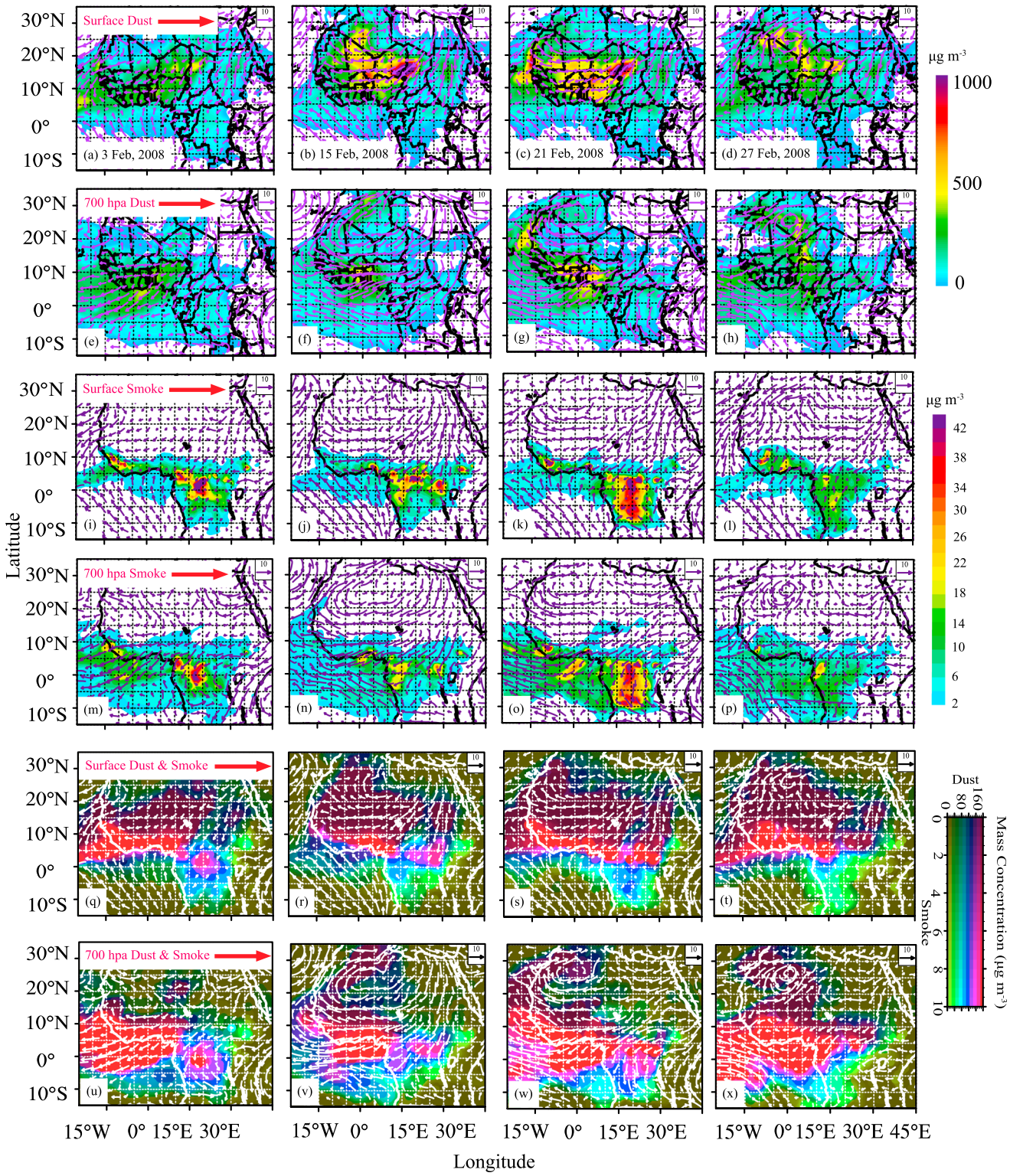

Figure 6. (a–d) Modeled dust mass concentration ($\mu g\, m^{-3}$) and wind vectors at the surface on 3, 15, 21, and 27 February 2008, respectively. (e–h) Same as Figures 6a–6d but for the 700 hPa layer. (i–l) Same as Figures 6a–6d but for modeled smoke. (m–p) Same as Figures 6a–6d but for modeled smoke and wind patterns at the 700 hPa layer. (q–t) Same as Figures 6a–6d but color-shaded according to the corresponding paired smoke versus dust mass concentration (with legend shown on the bottom right). (u–x) Same as Figures 6q–6t but for 700 hPa.

25°E) (Figure 5e). The WRF-Chem-simulated distributions of columnar total mineral dust and smoke mass (Figure 5i), mineral dust mass only (Figure 5m), and smoke mass only (Figure 5q) indicate that such AOD spatial distribution pattern reflects the mineral dust and smoke transport. The smoke-only simulation (Figure 5q) shows a significant amount of smoke loading in the Congo Basin, which is consistent with what can be inferred from MODIS AOD retrieval image (Figure 5e), though only partially visible in the true color image due to the overwhelming presence of clouds over this region. Near the surface, mineral dust is transported to the southwest by the northeasterlies and mixes with smoke over the central Sahel region (Figure 6a), while smoke is transported by the southerly wind along the west Gulf of Guinea to mix with the mineral dust over the equatorial coastal Atlantic Ocean (Figure 6i). However, over the north of Congo Basin, the smoke is confined by the convergence (ITCZ) around the smoke source region near the surface. Overall, near the surface, mineral dust is dominant north of 10°N, whereas there is mineral dust and smoke mixing between the equator and 10°N, decreasing to less mineral dust and more smoke over and south of the equator (Figure 6q). By comparison, at the middle troposphere (700 hPa), the southerly wind along the west of the Gulf of Guinea is replaced by the northeasterly wind, and hence, more mineral dust is transported to mix with smoke over the Atlantic Ocean, as can be clearly seen in Figures 6e and 6m. The mixing of mineral dust and smoke at this middle tropospheric layer is expanded southward to 5°S, which contrasts with the mixing pattern near the surface whose southern limit is close to the equator.

[32] The second largest smoke event over the Sahel region during 15 February 2008 was recorded at the AERONET sites (Figures 3a and 3g, pink shadow) and was also manifested in a large impact of smoke aerosols on the WRF-Chem-simulated AOD. The distribution of MODIS fire counts in the second smoke event is similar to that of the first one, which is mainly concentrated between the equator and 15°N (Figure 5b). North of 5°N, the occurrence of a stronger high-pressure system centers over the Sahara desert, resulting in the spread of dust over a larger area (Figures 5j and 5n versus Figures 5i and 5m). However, south of 5°N, the wind pattern near the surface and smoke distribution are both similar to those of 3 February over the north (Figure 5r versus Figure 5q). Near 5°N, the wind is shifted to a southeasterly flow (Figure 5r) associated with the northward movement of the ITCZ toward 5°N (Figure 5v versus 5u). The corresponding precipitation around this area and the wind shift suppress the mineral dust transport to the south at both surface and 700 hPa (Figures 6b and 6f versus Figures 6a and 6e). Furthermore, the southeasterlies associated with this strong high-pressure system at 700 hPa over the area of 5°S–15°S, 15°E–30°E (Figure 6f) differ with the northwesterly flow that occurred on 3 February (Figure 6e), which makes a big difference in transporting the smoke event over the north of the Congo Basin. Under this influence, smoke particles are transported to the far north over the western Saharan desert coast, but the southward transport of mineral dust is limited to the Gulf of Guinea. Consequently, the areas where mineral dust and smoke are well mixed (areas with bright red) are reduced at both the surface and midtroposphere (Figures 6r and 6v).

[33] The third event on 21 February was mainly dominated by mineral dust. The number of MODIS fire counts appears to be less than the previous two events during the daytime but more during the nighttime (Figure 5c versus Figures 5a and 5b). Also, more fires are detected in the Congo Basin. Near the surface, the high-pressure system that occurred on 15 February (Figure 5o) had moved westward to the northwest of the Sahara desert near Atlas Mountains (Figure 5n). Because of this western movement, part of the dust particles were advected over Niger, Mali, and Mauritania to the northwest of Sahara desert (Figure 5o). However, AOD was still quite high at the northern rim of the Gulf of Guinea and extended further to the north compared with the previous events (Figures 5g and 5k). The smoke mass loading appears larger (Figure 5s) than those of the previous events (Figures 5q and 5r). The smoke originating near the Congo Basin is transported to the south, especially within the 700 hPa layer, due to the wind veering from northeasterlies to northerlies (Figures 6k and 6o). Overall, the mineral dust and smoke mixture moved westward near the surface (Figures 6c, 6k, and 6s) and southward at the 700 hPa layer (Figures 6g, 6o, and 6w).

[34] The fourth event happened on 27 February. Due to the continuous northern movement of the ITCZ, the precipitation belt also moved northward, resulting in less rainfall east of the Great Rift Valley (Figure 5x). Therefore, more fires were found near the Congo Basin (Figure 5d), but overall smoke mass loading (Figure 5t) is similar to that on 21 February. The area of large AODs expanded northward, almost covering the whole northwestern parts of the Sahara desert (Figure 5h). This expansion is mainly contributed by dust. Because of the strengthening of a surface high-pressure system over the east of the Sahara, a great trough was formed over Niger and Nigeria (Figure 5l). The mineral dust transport pattern changed significantly (Figures 5l and 5p) compared to the situation on 21 February (Figures 5k and 5o). The mineral dust was advected to the north straight from its source region near Lake Chad (Figure 5p), which is different from the transport pattern observed on earlier dates of first flowing to the west and then to the north (Figure 5o). Such northward transport is more dominant at the surface (Figure 6d) than at 700 hPa (Figure 6h). Again, due to the northern movement of the ITCZ, the mixture of mineral dust and smoke also moved directly northward (Figure 6t). At the 700 hPa layer, the aerosols seemed to have migrated farther south to the Gulf of Guinea compared to the 21 February event, suggesting that the aerosols may have been lifted up higher in altitude. This resulted in a deck of the mixed smoke and mineral dust forming over the Gulf of Guinea, creating a special phenomenon of aerosols above cloud. Section 4.7 will provide a more detailed analysis of this phenomenon.

[35] Besides individual smoke and mineral dust events, monthly averages of column smoke and mineral dust also show their horizontal distribution (Figure 7). Mineral dust is mainly confined to the north of the Gulf of Guinea, between the equator and 20°N and west of 20°E (Figure 7b). The smoke is located from the northwest of Congo Basin to the east of the Gulf of Guinea (Figure 7c).

4.4. Aerosol Vertical Distribution and Smoke Injection Height

[36] The simulated aerosol vertical profiles were verified using CALIOP-based Level 1 and Level 2 aerosol products.

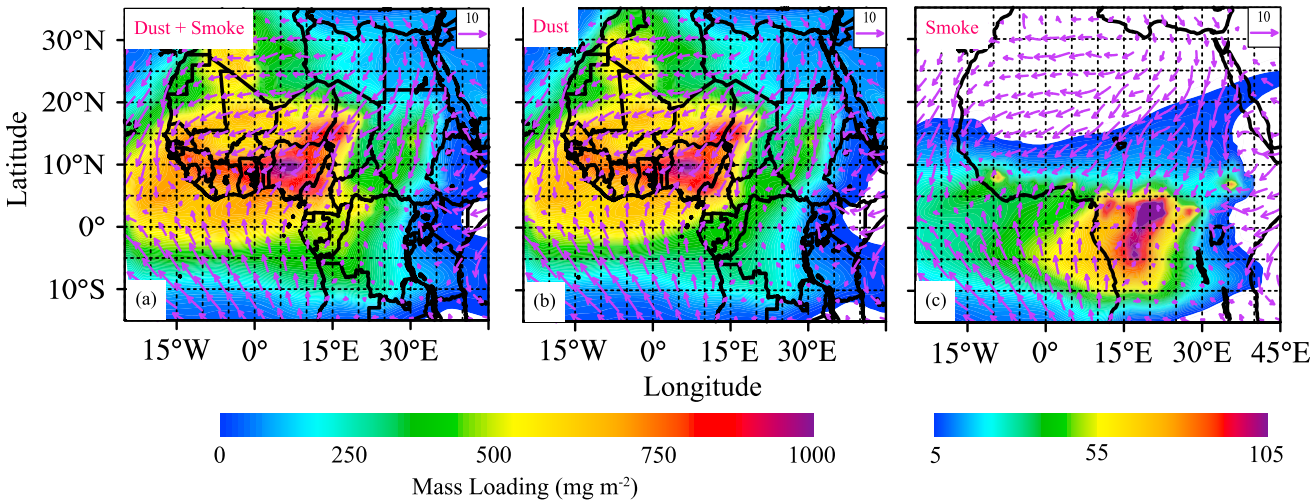

Figure 7. (a) Modeled monthly (February 2008) column dust and smoke mass loading, overlaid with surface wind patterns. (b) Same as Figure 7a but for dust. (c) Same as Figure 7a but for smoke.

First, they were visually compared with the CALIOP-based total attenuated backscatter (532 nm) Level 1 product, as well as the aerosol extinction coefficient (532 nm) and depolarization ratio Level 2 products. Then, we located the CALIPSO ground track within the main model domain (red line on the inset map in Figures 8d–8f). The selected grids of the WRF-Chem simulations match the CALIPSO ground track closely. The total attenuated backscatter (532 nm) profiles show that cirrus clouds are distributed at high altitudes (mostly above 10 km) whereas aerosol is located near the surface (below 5 km; Figures 8a–8c). Most of the cirrus is thin enough to allow the CALIOP lidar signal to pass through and reach the surface (Figures 8a and 8b), although some thick cirrus also exists and can block the lidar signal from reaching the surface, preventing the aerosol beneath from being detected by CALIOP (Figure 8c). High aerosol concentrations can be distinguished based on the relative color-coded values of the extinction coefficient (cloud is gray coded) (Figures 8d–8f). It is noted that some aerosols are located above certain low clouds (Figures 8d and 8f, marked with ellipses). This phenomenon will be analyzed further below. The model simulations were conducted to perform two sensitivity experiments using injection heights of 650 m and 2000 m (Figures 8j–8l and 8m–8o for an injection height of 650 m representing mineral dust + smoke and smoke only, respectively; Figures 8p–8r for an injection height of 2000 m). Compared to CALIOP observations, the simulation based on the injection height of 650 m can capture the smoke vertical distribution more accurately, suggesting that the smoke injection height around the Sahel region is on the order of 650 m. The injection height used in the model not only influences the vertical distribution of smoke but also affects its horizontal dispersion. The simulation with injection height of 650 m also has a closer resemblance to the horizontal distribution portrayed by the CALIOP profiles.

[37] Given the limited spatial coverage of CALIOP, it is not straightforward to compare the model with the statistics of CALIOP data. Instead, the CALIOP ground tracks within the nested model domain are selected to test the robustness of our model simulations of aerosol vertical distribution during February 2008 (Figure 9a); multiple-year analysis of CALIOP data in 2007, 2009, 2010, and 2011 (Figures 9d–9g) and their averages (Figure 9h) shows that the profile of aerosols in February 2008 is representative for this region. In addition, most smoke particles also reside in the nested model domain (shown as the blue dashed square in Figure 1b). To compare the CALIOP observation and model simulation, both data are interpolated and binned at a vertical resolution of 300 m (equivalent to five vertical intervals in the CALIOP Level 2 aerosol products).

[38] Figure 9a shows the CALIOP layer AOD statistical vertical profile. The layer AOD value is consistent at about 0.012 from the surface to 1.8 km altitude, illustrating that the aerosols are well mixed near the surface. As the altitude increases, the layer AOD decreases, except at the height around 5 km, where it shows a sudden increase likely due to cloud contamination. From Figures 8d–8f, it is obvious that there are indeed clouds around this height. In addition, if we count each atmospheric column that CALIOP Level 2 products (5 km spatial resolution along the horizontal) cover as one data sample, we can find that the probability (normalized to all samples) for CALIOP to detect an aerosol-contaminated 300 m thick layer in an atmospheric column is ~8% from surface to 2.8 km (shown in Figure 9a as color-coded valid aerosol observation frequency). This probability decreases to 3% at 4.0 km and approaches zero when the altitude is above 4.2 km (Figure 9a), which, as expected, indicates the infrequent occurrence of aerosol layers in the middle to upper troposphere.

[39] The CALIOP layer AOD profile analysis was used to evaluate the model sensitivity to smoke injection height. Three injection heights were specified in the model, and the resulting simulations were analyzed statistically (Figure 9b). Figure 10b shows modeled smoke vertical profiles using injection heights of 500 m, 650 m, and 2000 m, showing that the injection height of 650 m renders best agreement with the

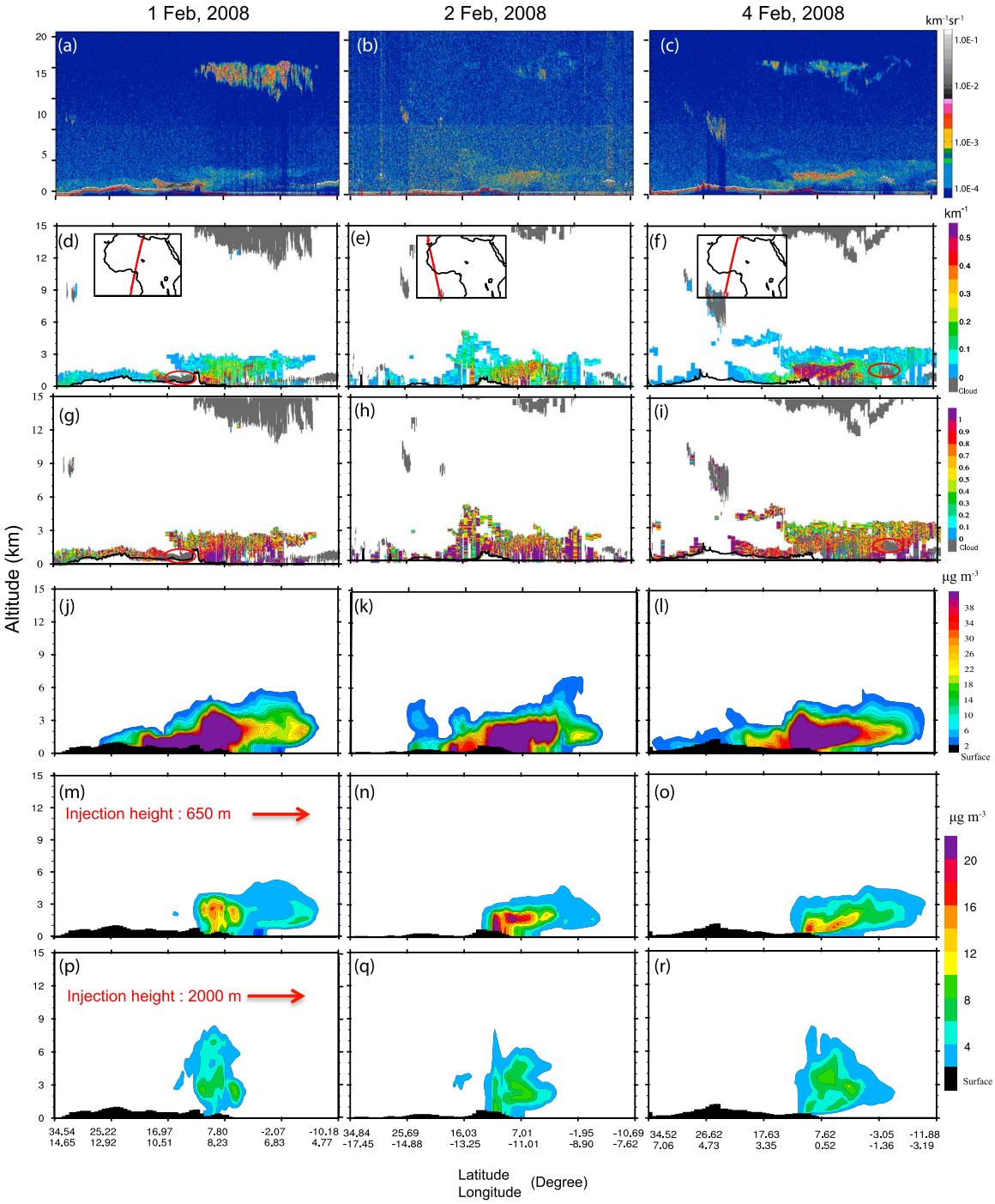

Figure 8. Intercomparison of CALIOP-derived vertical profile of total attenuated backscatter (532 nm, first row), aerosol extinction coefficient (second row), and depolarization ratio at 532 nm (third row) with the WRF-Chem-simulated vertical profiles of total (dust + smoke) aerosol concentration along the corresponding CALIPSO ground track with injection height of 0.65 km for smoke (fourth row), smoke concentration only (fifth row) with injection height of 0.65 km, and smoke concentration only with injection height of 2.0 km (sixth row). The dates are 1, 2, and 4 of February 2008 from the first column to the third column. Corresponding CALISPO ground tracks are shown in the inset maps (red curve) in the second row.

observation. By specifying an injection height of 500 m, most of the smoke is confined near the surface, whereas if the injection height is set to 2000 m, smoke is shifted to higher levels, leaving very little near the surface. Both injection height values result in smoke vertical distributions that are inconsistent with CALIOP observations. Figure 9c shows that most of the large layer AOD is located below 4 km. The frequency of occurrence of layer AODs larger

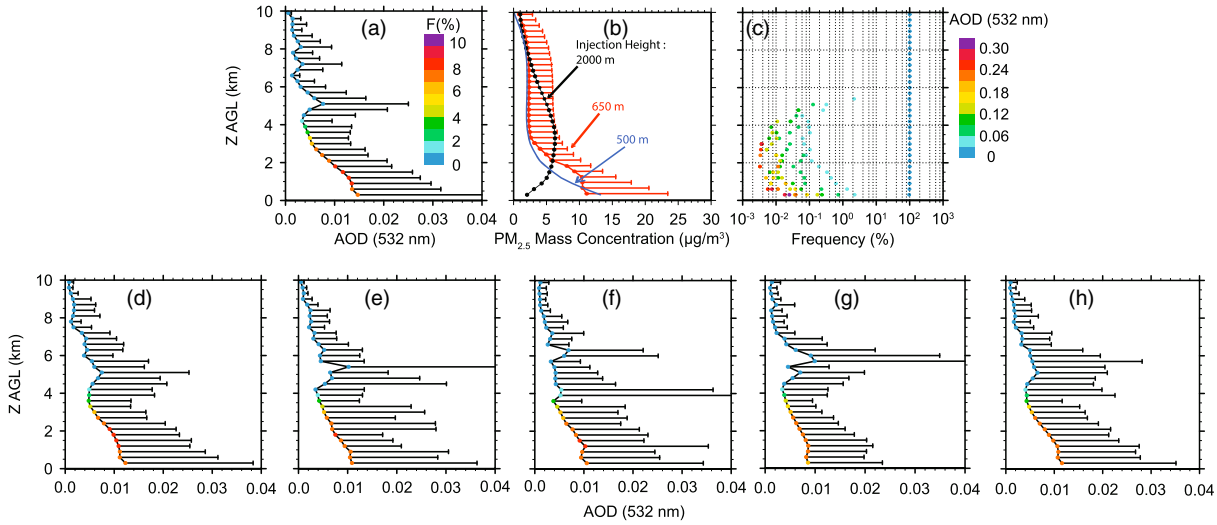

Figure 9. (a) Monthly averages of CALIOP-derived layered (300 m thick) AOD (532 nm) as a function of altitude above ground level (AGL) in the smoke source region in February 2008. (b) Similar to Figure 9a but for WRF-Chem-simulated $PM_{2.5}$ (e.g., smoke particle) mass concentration along the CALIPSO ground track with different injection heights (500 m, 650 m, and 2000 m). The length of the horizontal bar at each layer represents the 1 standard deviation for all valid aerosol optical depth (AOD) data sampled at that layer. (c) Frequency of CALIOP-derived AOD in each 300 m layer with different ranges. The frequency of AOD in each layer is denoted by color solid circles. The range is from 0.0 to 0.3 with intervals of 0.03. (d–g) Same as Figure 9a but for 2007, 2009, 2010, 2011, and the 2007–2011 average, respectively.

than 0.3 is about 0.1% around the surface, and most (90%) of the layer AODs (0–0.06) are very small.

4.5. Smoke and Mineral Dust Vertical Mixing

4.5.1. Monthly Statistics

[40] The vertical distributions of smoke and mineral dust are shown in Figure 10, overlaid with wind fields. Considering the vertical transport and mixing of smoke and mineral dust, three different cross sections along west-east and north-south are selected near the smoke and mineral dust source region, respectively. Three east-west cross sections are at latitudes 5.0°S, 5.0°N, and 15.0°N (Figures 10a–10c, red lines). Three north-south cross sections are at longitudes 35.0°E, 15.0°E, and 5.0°W (Figures 10d–10f, blue lines).

[41] These plots help address a few relevant questions. First, how do the smoke and mineral dust mix along the north

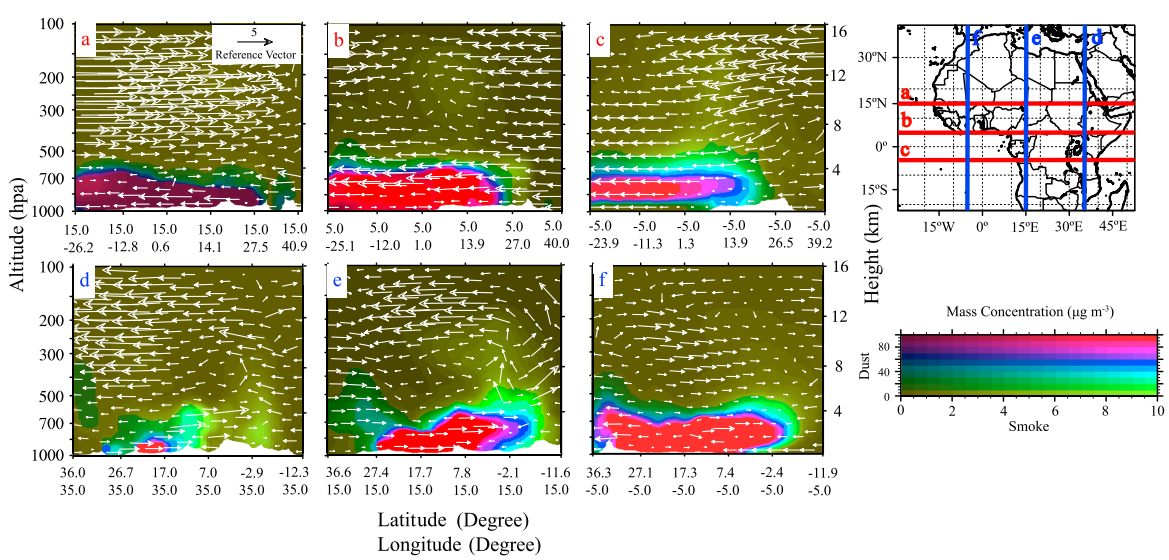

Figure 10. (a–c) Smoke and dust mass concentration in three vertical cross sections passing through the horizon at −5.0°N, 5.0°N, and 15.0°N, respectively. (d–f) Smoke and dust mass concentration in three vertical cross sections passing through the longitudes of −5.0°E, 15.0°E, and 35.0°E, respectively. Arrows represent wind speeds (m s^{-1}) and directions. (upper right) Positions of these cross sections on the map. (bottom right) The color bar.

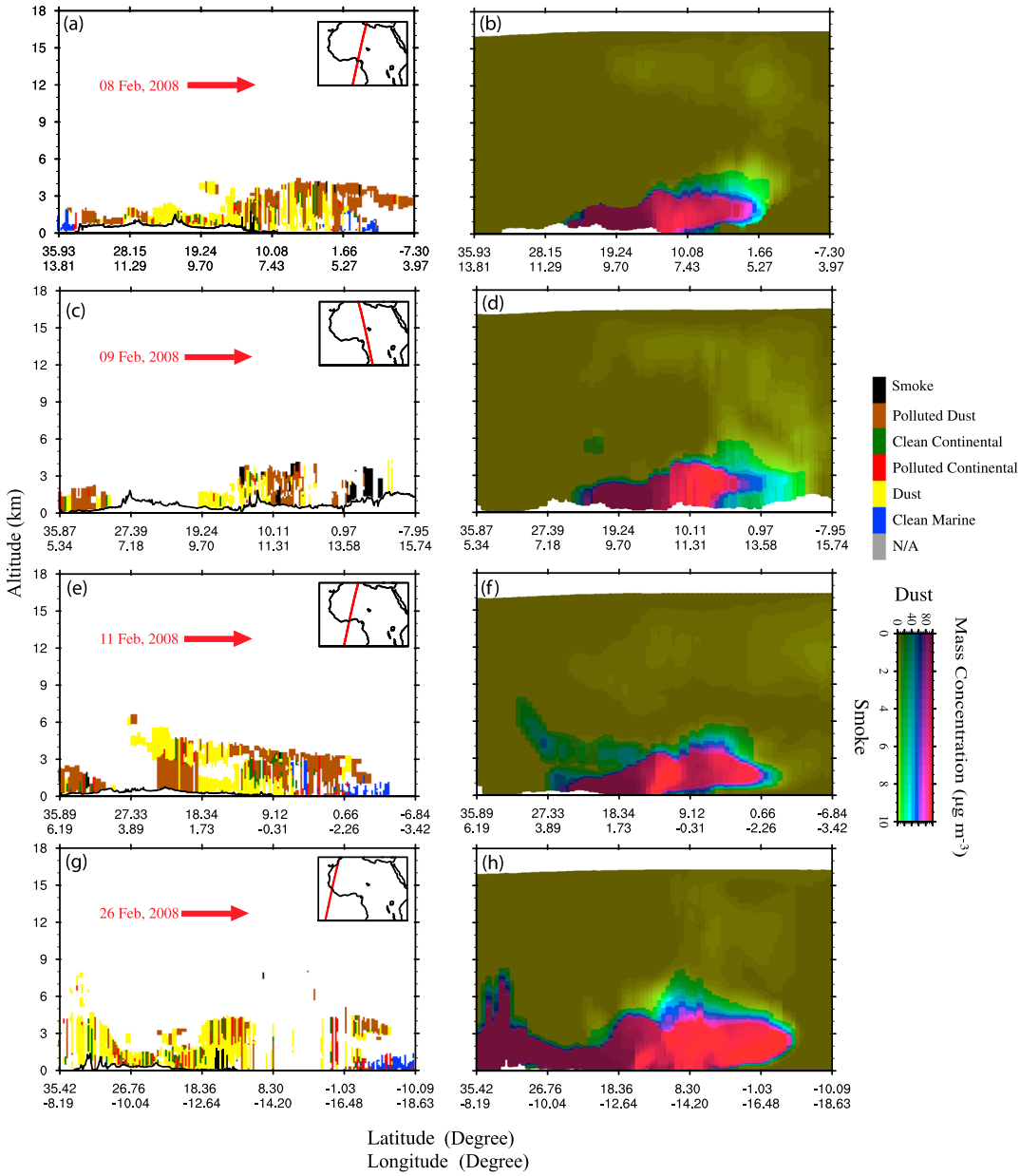

Figure 11. (a) CALIOP-derived vertical feature mask on 8 February 2008; the inset on the upper right shows the ground track of CALIPSO (denoted as the red curve). (b) Vertical cross section along the CALIOP ground track shown in Figure 11a, color-shaded according to the paired smoke and dust mass concentrations. (c, e, g) Same as Figure 11a but for 9, 11, and 26 February 2008. (d, f, h) Same as Figure 11b but for 9, 11, and 26 February 2008.

to south axis? For the northernmost cross section, mineral dust mass concentration is much more, but smoke mass concentration is far less, because this cross section passes through the mineral dust source region (Figure 10a). The flow pattern is easterly near the surface but westerly in the higher layer. Near the surface, the trade winds are northeasterly. They carry mineral dust from the dust source region to the west coast of the Sahara desert. In the midtroposphere, westerlies prevail at 15.0°N. Mineral dust is lifted up while being transported from its source region to the west. Small amounts of smoke are found at the west side of this cross section at altitudes of 2–3 km, due to the northward propagation of smoke over the Gulf of Guinea.

[42] For the east-west cross section passing through the smoke source region (at 5.0°N), the flow patterns are significantly different from those of the 15.0°N cross section (Figure 10b). Surface winds are westerly over the Gulf of Guinea, but easterly winds prevail over the continent. The resulting convergence hinders the smoke transport to the ocean. From 850 hPa to 400 hPa, the wind is easterly and carries smoke from its source region to the ocean. It helps to form a smoke deck over the Gulf of Guinea. Above 400 hPa, a convergence is produced by the westerly and easterly winds.

[43] Along the 5.0°S cross section, the wind is easterly from the surface to the higher layer. The wind speed is much higher over the Atlantic Ocean than over the continent, which

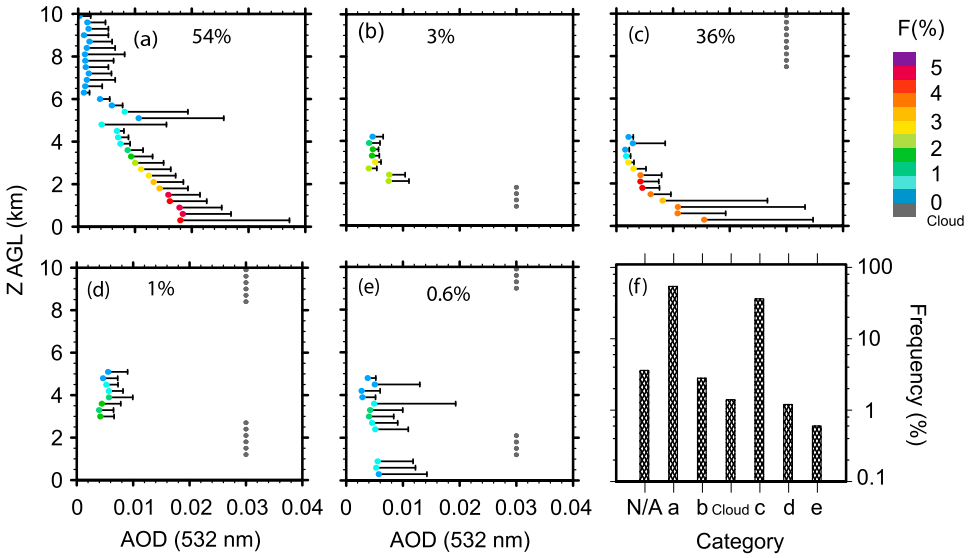

Figure 12. Monthly averages of CALIOP-derived layered (300 m thick) AOD (532 nm) as a function of altitude (within 10 km) above ground level (AGL), categorized according to the relative vertical positions of aerosol and cloud layers. These categories include the following: (a) cloud-free in the whole atmospheric column sampled by the CALIOP, (b) aerosol above cloud, (c) aerosol below cloud, (d) aerosol between two cloud layers, and (e) cloud-aerosol-cloud-aerosol vertical structure. The frequency of AOD in each layer is denoted by filled colored circles in Figures 12a–12e; also shown are standard deviations of AOD in each layer. The filled gray circles only represent the position of cloud. (f) Distribution of frequency for each vertical profile category, including no valid measurements of aerosol and cloud over the whole atmospheric column (denoted as N/A) and cloud layer with no aerosol layer in the column (denoted as cloud).

is due to reduced surface friction over the ocean. Smoke can be transported to levels near 8 km while mineral dust is lifted to around 4 km (Figure 10c). Smoke is lifted up especially over the smoke source region north of the Congo Basin. The flow patterns are easterly along the vertical from east to west, which are trade winds south of the ITCZ. Nevertheless, a high mass concentration of mineral dust is located over the Gulf of Guinea and is well mixed with smoke. These dust aerosols are transported from the north (Figure 10f). In addition, smoke shows a higher concentration at higher levels over the east of the Gulf of Guinea and lower concentrations to the west.

[44] Additional insight can be derived from the characteristics of the smoke and mineral dust mixture along the north-south cross sections (Figures 10d–10f). For the easternmost cross section (Figure 10d), both mineral dust and smoke concentrations are less than 10 μg/m^3 and 40 μg/m^3, respectively, except over the area around the northeast of Sudan, which is near the mineral dust source region. The flow pattern is northerly near the surface but southerly in the upper layers. The ITCZ is situated around the southeast of Kenya, with a significant updraft flow that causes the smoke to be appreciably uplifted near this region.

[45] In the 15.0°E cross section (Figure 10e), which passes through the smoke source region, the smoke concentration is much higher near the surface (more than 10 μg/m^3). Considering the influence of the ITCZ near the equator, smoke and mineral dust can be lifted to altitudes of 10 km and 5 km, respectively, near southwestern Democratic Republic of the Congo. The Hadley cell is significant over this cross section.

[46] Further to the west, the flow pattern is southerly from Algeria to Cote d'Ivoire but northerly toward the north of Algeria as well as over the Gulf of Guinea. However, at the middle layer, the flow pattern is northerly but changes to southerly again at the higher layer. Due to this wind shear, a deck of aerosol particles is generated above the Gulf of Guinea. All of these demonstrate a special phenomenon, aerosol above cloud, which will be discussed in detail in section 4.6.

[47] All the cross sections show that smoke is above mineral dust statistically, which is in agreement with the findings of *Haywood et al.* [2008] from airborne measurements. However, different cross sections show mineral dust and smoke at a range of different altitudes, although as discussed below, in several cases, mineral dust and smoke are well mixed, and dust can sometimes even be above a smoke layer.

4.5.2. Analysis of Well-Mixed Cases

[48] Four cases are shown regarding the relative position of aerosol subtypes from CALIOP observations (Figures 11a, 11c, 11e, and 11g) and WRF-Chem-simulated relative position of smoke and mineral dust along the CALIPSO ground track (Figures 11b, 11d, 11f, and 11h). On 8 February, patches of smoke are located north of 10°N (north of Nigeria). They are distributed from the surface to 2 km, mixing with dust (Figures 11a and 11b). The smoke mass concentration decreases with height. Similar to 8 February, smoke is near the surface and is well mixed with polluted dust or dust on 9, 11, and 26 February (Figures 11c–11h), even around 15°N. This phenomenon is different from the conceptual model presented by *Haywood et al.* [2008], which illustrated smoke above dust north of 10°N. However, on 26 February, the smoke mass concentration is elevated in the layers that lie from 4 km to 6 km. Considering the atmospheric circulation patterns and the ITCZ, this increase of smoke is a result of accumulation and transport from smoke

source regions, rather than from local combustion. Both CALIOP aerosol subtypes observations and WRF-Chem simulations show that smoke is well mixed with mineral dust north of 10°N.

4.6. Aerosol and Cloud Relative Vertical Position From CALIOP Observations

[49] As we see from Figures 8d to 8f, smoke and dust particles can be above clouds, which increase their effective forcing because light strongly reflected by clouds is again absorbed and scattered by overlying smoke and dust. Considering this particular phenomenon, we use CALIOP Level 2 products in February 2008 to analyze the vertical profile of aerosol and cloud relative position (from surface to 10 km). Figure 12 shows four categories of typical aerosol-cloud layering patterns (from top to bottom): (1) aerosol only (Figure 12a), (2) aerosol-cloud (Figure 12b), (2) cloud-aerosol (Figure 12c), (3) cloud-aerosol-cloud (Figure 12d), and (4) cloud-aerosol-cloud-aerosol (Figure 12e). Statistics suggests that the aerosol-only case is dominant over the NSSA region, whose contribution is around 54% for category 1 (Figure 12f). Cloud layers are on average below 2 km, while aerosol layers are between 2 km and 4.5 km for category 2, whose occurrence constitutes about 3% of all the observed cases. Most commonly observed is category 3, which occurs 36% of the time and whose cloud layer is very high (above 7.5 km). For category 4, the aerosol is constrained between two cloud layers, and its percentage is around 1%. Least common is category 5 with an occurrence of only about 0.6%. In this category, the cloud can be as low as 1 km with aerosol below and above it. The combined percentage of categories 2, 4, and 5 is about 5%. Statistical representation of various types of relative spatial arrangements of aerosol and cloud layers is needed in climate models for reliable simulation of semidirect effect of absorbing aerosols [*Hansen et al.*, 1997].

5. Conclusions and Discussions

[50] Based on WRF-Chem simulations using the FLAMBE smoke emission inventory, we studied the characteristics of the smoke transport pathways in the Sahel region during February 2008 and found that smoke transport and its mixing with dust are influenced by the combined effects of trade winds, subtropical highs, and migration of the ITCZ. The WRF-Chem simulation is found to agree well with MODIS, AERONET, and CALIOP observations in terms of the spatio-temporal variation of smoke and dust distribution in the atmosphere. The main conclusions are as follows:

[51] 1. The time series and geographic distributions of WRF-Chem-simulated mineral dust and smoke mass loadings are in good agreement with the AERONET total AODs and coarse-mode AODs. Their correlation coefficients are on average around 0.8 over six AERONET sites. In total, four polluted events in February were identified.

[52] 2. Smoke transport over West Africa is affected by the ITCZ, subtropical highs, trade winds, and topography. At the surface, the smoke is confined mainly between 10°N and the equator, whereas at 700 hPa, it can extend from 10°N to 10°S. Further extension is bounded by the effects of precipitation in the south and high-pressure systems in the north.

[53] 3. In contrast to many previous studies that used an injection height of 2 km in chemistry transport models [*Liousse et al.*, 1996], a sensitivity experiment shows that an injection height of 0.65 km gives the best agreement between the model-simulated profile of aerosols and the corresponding CALIOP observations.

[54] 4. CALIOP detects that most of the aerosol mass loading is below 4 km. Consistent with CALIOP observations, the aerosol particles simulated by WRF-Chem have relatively uniform concentrations from surface to 1.5 km, which then decrease with height from 1.5 km to 4 km.

[55] 5. While smoke layers can be often found above dust or dust-smoke layers, we also found cases where a smoke layer was below a dust layer. The WRF-Chem simulation shows that these mixed layers can be transported to the Atlantic east coast and then turn east to the northern part of the Sahara desert.

[56] 6. Analysis of the relative positions of cloud and aerosol layers revealed that, among all the cases where CALIOP detected aerosol layers, the cases for aerosol above cloud or between cloud layers are about 5% during February 2008.

[57] Since dust and smoke are both light-absorbing aerosols, their vertical distribution in the atmosphere, including their position with respect to clouds, is critical for us to understand their radiative feedback and needs to be reliably represented in the model. To achieve this goal, constraints from satellite observations such as CALIOP, as illustrated in this paper, are highly valuable. Reliable simulation of the timing and 3D distribution of smoke and dust particles in the Sahel region, as shown in this study, therefore provide the basis for our next step to estimate smoke direct and indirect radiative forcing and quantify their feedback on meteorology and precipitation in this region.

[58] **Acknowledgments.** This research was supported by the Science Mission Directorate of the National Aeronautics and Space Administration (NASA) as part of the Interdisciplinary Studies (IDS) conducted through the Radiation Sciences Program managed by Hal B. Maring. Part of the computational support in this research is also provided by the Holland Computing Center of the University of Nebraska. J. Wang also thank Dr. Robert Oglesby and Dr. Qi (Steve) Hu at the University of Nebraska—Lincoln for their constructive comments.

References

Ackermann, I., H. Hass, M. Memmesheimer, A. Ebel, F. Binkowski, and U. Shankar (1998), Modal aerosol dynamics model for Europe: Development and first applications, *Atmos. Environ.*, *32*, 2981–2999.

Capes, G., B. Johnson, G. McFiggans, P. Williams, J. Haywood, and H. Coe (2008), Aging of biomass burning aerosols over West Africa: Aircraft measurements of chemical composition, microphysical properties, and emission ratios, *J. Geophys. Res.*, *113*, D00C15, doi:10.1029/2008JD009845.

Chen, F., and J. Dudhia (2001), Coupling an advanced land surface-hydrology model with the Penn State-NCAR MM5 modeling system. Part I: Model implementation and sensitivity, *Mon. Weather Rev.*, *129*, 569–585.

Chou, M. D., M. J. Suarez, C. H. Ho, M. M. H. Yan, and K. T. Lee (1998), Parameterizations for cloud overlapping and shortwave single-scattering properties for use in general circulation and cloud ensemble models, *J. Clim.*, *11*, 202–214.

Donnelly, J., and J. Woodruff (2007), Intense hurricane activity over the past 5,000 years controlled by El Nino and the West African monsoon, *Nature*, *447*, 465–468.

Dubovik, O., A. Smirnov, B. N. Holben, M. D. King, Y. J. Kaufman, T. F. Eck, and I. Slutsker (2000), Accuracy assessment of aerosol optical properties retrieval from AERONET sun and sky radiance measurements, *J. Geophys. Res.*, *105*, 9791–9806.

Eck, T., B. Holben, J. Reid, O. Dubovik, A. Smirnov, N. O'Neill, I. Slutsker, and S. Kinne (1999), Wavelength dependence of the optical depth of biomass burning, urban, and desert dust aerosols, *J. Geophys. Res.*, *104*(D24), 31,333–31,349.

Fast, J., W. Gustafson Jr, R. Easter, R. Zaveri, J. Barnard, E. Chapman, G. Grell, and S. Peckham (2006), Evolution of ozone, particulates, and

aerosol direct radiative forcing in the vicinity of Houston using a fully coupled meteorology-chemistry-aerosol model, *J. Geophys. Res.*, *111*, D21305, doi:10.1029/2005JD006721.

Franca, J., J. Brustet, and J. Fontan (1995), Multispectral remote sensing of biomass burning in West Africa, *J. Atmos. Chem.*, *22*, 81–110.

Freeborn, P. H., M. J. Wooster, and G. Roberts (2011), Addressing the spatiotemporal sampling design of MODIS to provide estimates of the fire radiative energy emitted from Africa, *Remote Sens. Environ.*, *115*, 475–489.

Freeborn, P. H., M. J. Wooster, G. Roberts, B. D. Malamud, and W. D. Xu (2009), Development of a virtual active fire product for Africa through a synthesis of geostationary and polar orbiting satellite data, *Remote Sens. Environ.*, *113*(8), 1700–1711.

Giglio, L., J. Descloitres, C. O. Justice, and Y. J. Kaufman (2003), An enhanced contextual fire detection algorithm for MODIS, *Remote Sens. Environ.*, *87*, 273–282.

Ginoux, P., M. Chin, I. Tegen, J. Prospero, B. Holben, O. Dubovik, and S. Lin (2001), Sources and distributions of dust aerosols simulated with the GOCART model, *J. Geophys. Res.*, *106*, 20,255–20,273.

Greed, G., J. Haywood, S. Milton, A. Keil, S. Christopher, P. Gupta, and E. Highwood (2008), Aerosol optical depths over North Africa: 2. Modeling and model validation, *J. Geophys. Res.*, *113*, D00C05, doi:10.1029/2007JD009457.

Grell, G., and D. Devenyi (2002), A generalized approach to parameterizing convection combining ensemble and data assimilation techniques, *Geophys. Res. Lett.*, *29*(14), 1693, doi:10.1029/2002GL015311.

Grell, G., S. Peckham, R. Schmitz, S. McKeen, G. Frost, W. Skamarock, and B. Eder (2005), Fully coupled 'online' chemistry within the WRF model, *Atmos. Environ.*, *39*(37), 6957–6975.

Hansen, J., M. Sato, and R. Ruedy (1997), Radiative forcing and climate response, *J. Geophys. Res.*, *102*(D6), 6831–6864, doi:10.1029/96JD03436.

Haywood, J., J. Pelon, P. Formenti, N. Bharmal, M. Brooks, G. Capes, P. Chazette, C. Chou, S. Christopher, and H. Coe (2008), Overview of the dust and biomass-burning experiment and African Monsoon Multidisciplinary Analysis Special Observing Period-0, *J. Geophys. Res.*, *113*, D00C17, doi:10.1029/2008JD010077.

Holben, B., et al. (2001), An emerging ground-based aerosol climatology: Aerosol optical depth from AERONET, *J. Geophys. Res.*, *106*, 12,067–12,097.

Holben, B. N., et al. (1998), AERONET—A federated instrument network and data archive for aerosol characterization, *Remote Sens. Environ.*, *66*, 1–16.

Hong, S. Y., J. Dudhia, and S. H. Chen (2004), A revised approach to ice microphysical processes for the bulk parameterization of clouds and precipitation, *Mon. Weather Rev.*, *132*, 103–120.

Hong, S. Y., Y. Noh, and J. Dudhia (2006), A new vertical diffusion package with an explicit treatment of entrainment processes, *Mon. Weather Rev.*, *134*, 2318–2341.

Hsu, N. C., T. Si-Chee, M. D. King, and J. R. Herman (2006), Deep blue retrievals of asian aerosol properties during ACE-Asia, *Geosci Remote Sens. IEEE Transactions*, *44*, 3180–3195.

Hyer, E. J., J. S. Reid, E. M. Prins, J. P. Hoffman, C. C. Schmidt, J. I. Miettinen, and L. Giglio (2013), Patterns of fire activity over Indonesia and Malaysia from polar and geostationary satellite observations, *Atmos. Res.*, *122*, 504–519.

Ichoku, C., L. Giglio, M. J. Wooster, and L. A. Remer (2008), Global characterization of biomass-burning patterns using satellite measurements of fire radiative energy, *Remote Sens. Environ.*, *112*, 2950–2962.

Johnson, B. T., S. R. Osborne, J. M. Haywood, and M. A. J. Harrison (2008a), Aircraft measurements of biomass burning aerosol over West Africa during DABEX, *J. Geophys. Res.*, *113*, D00C06, doi:10.1029/2007JD009451.

Johnson, B. T., B. Heese, S. A. McFarlane, P. Chazette, A. Jones, and N. Bellouin (2008b), Vertical distribution and radiative effects of mineral dust and biomass burning aerosol over West Africa during DABEX, *J. Geophys. Res.*, *113*, D00C12, doi:10.1029/2008JD009848.

Kalnay, E., M. Kanamitsu, R. Kistler, W. Collins, D. Deaven, L. Gandin, M. Iredell, S. Sana, G. White, and J. Woollen (1996), The NCEP/NCAR 40-Year Reanalysis Project, *Bull. Am. Meteorol. Soc.*, *77*, 437–471.

Kaufman, Y. J., C. J. Tucker, and I. Fung (1990), Remote sensing of biomass burning in the tropics, *J. Geophys. Res.*, *95*, 9927–9939.

Kaufman, Y. J., D. Tanré, L. A. Remer, E. F. Vermote, A. Chu, and B. N. Holben (1997), Operational remote sensing of tropospheric aerosol over land from EOS moderate resolution imaging spectroradiometer, *J. Geophys. Res.*, *102*, 17,051–17,067.

Kaufman, Y. J., I. Koren, L. A. Remer, D. Rosenfeld, and Y. Rudich (2005a), The effect of smoke, dust, and pollution aerosol on shallow cloud development over the Atlantic Ocean, *Proc. Natl. Acad. Sci. U. S. A.*, *102*, 11,207–11,212.

Kaufman, Y., I. Koren, L. Remer, D. Tanré, P. Ginoux, and S. Fan (2005b), Dust transport and deposition observed from the Terra-Moderate Resolution Imaging Spectroradiometer (MODIS) spacecraft over the Atlantic Ocean, *J. Geophys. Res.*, *110*, D10S12, doi:10.1029/2003JD004436.

Kistler, R., W. Collins, S. Saha, G. White, and J. Woollen (2001), The NCEP-NCAR 50-Year Reanalysis: Monthly Means CD-ROM and Documentation, *Bull. Am. Meteorol. Soc.*, *82*, 247–267.

Lau, K. M., K. M. Kim, Y. C. Sud, and G. K. Walker (2009), A GCM study of the response of the atmospheric water cycle of West Africa and the Atlantic to Saharan dust radiative forcing, *Ann. Geophys.*, *27*, 4,023–4,037, doi:10.5194/angeo-27-4023-2009.

Levy, R. C., L. A. Remer, S. Mattoo, E. F. Vermote, and Y. J. Kaufman (2007), Second-generation operational algorithm: Retrieval of aerosol properties over land from inversion of Moderate Resolution Imaging Spectroradiometer spectral reflectance, *J. Geophys. Res.*, *112*, D13211, doi:10.1029/2006JD007811.

Levy, R., L. Remer, R. Kleidman, S. Mattoo, C. Ichoku, R. Kahn, and T. Eck (2010), Global evaluation of the Collection 5 MODIS dark-target aerosol products over land, *Atmos. Chem. Phys.*, *10*, 10,399–10,420.

Liousse, C., J. E. Penner, C. Chuang, J. J. Walton, H. Eddleman, and H. Cachier (1996), A global three-dimensional model study of carbonaceous aerosols, *J. Geophys. Res.*, *101*, 19,411–19,432.

Liu, Z., M. A. Vaughan, D. M. Winker, C. A. Hostetler, L. R. Poole, D. Hlavka, W. Hart, and M. McGill (2004), Use of probability distribution functions for discriminating between cloud and aerosol in lidar backscatter data, *J. Geophys. Res.*, *109*, D15202, doi:10.1029/2004JD004732.

Liu, Z., M. Vaughan, D. Winker, C. Kittaka, B. Getzewich, R. Kuehn, A. Omar, K. Powell, C. Trepte, and C. Hostetler (2009), The CALIPSO lidar cloud and aerosol discrimination: Version 2 algorithm and initial assessment of performance, *J. Atmos. Oceanic Technol.*, *26*, 1198–1213.

Malavelle, F., M. Mallet, V. Pont, C. Liousse, and F. Solmon (2011), Long-term simulations (2001–2006) of biomass burning and mineral dust optical properties over West Africa: Comparisons with new satellite retrievals, *Atmos. Chem. Phys. Discuss.*, *11*, 28,587–28,626.

Marey, H. S., J. C. Gille, H. M. El-Askary, E. A. Shalaby, and M. E. El-Raey (2011), Aerosol climatology over Nile Delta based on MODIS, MISR and OMI satellite data, *Atmos. Chem. Phys.*, *11*(20), 10,637–10,648.

Mlawer, E. J., S. J. Taubman, P. D. Brown, M. J. Iacono, and S. A. Clough (1997), Radiative transfer for inhomogeneous atmospheres: RRTM, a validated correlated-k model for the longwave, *J. Geophys. Res.*, *102*, 16,663–16,682.

Myhre, G., T. K. Berntsen, J. M. Haywood, J. K. Sundet, B. N. Holben, M. Johnsrud, and F. Stordal (2003a), Modelling the solar radiative impact of aerosols from biomass burning during the Southern African Regional Science Initiative (SAFARI-2000) experiment, *J. Geophys. Res.*, *108*(D13), 8501, doi:10.1029/2002JD002313.

Myhre, G., A. Grini, J. M. Haywood, F. Stordal, B. Chatenet, D. Tanré, J. K. Sundet, and I. S. A. Isaksen (2003b), Modeling the radiative impact of mineral dust during the Saharan Dust Experiment (SHADE) campaign, *J. Geophys. Res.*, *108*(D18), 8579, doi:10.1029/2002JD002566.

Peterson, D., and J. Wang (2013), A Sub-pixel-based calculate of fire radiative power from MODIS observations: 2. Sensitivity analysis and potential fire weather application, *Remote Sens. Environ.*, *129*, 231–249.

Peterson, D., J. Wang, C. Ichoku, E. Hyer, and V. Ambrosia (2013), A Sub-pixel-based calculate of fire radiative power from MODIS observations: 1. Algorithm development and validation, *Remote Sens. Environ.*, *129*, 262–279.

Prasad, A. K., H. El-Askary, and M. Kafatos (2010), Implications of high altitude desert dust transport from Western Sahara to Nile Delta during biomass burning season, *Environ. Pollution*, *158*(11), 3385–3391.

Price, J. F., J. Morzel, and P. P. Niiler (2008), Warming of SST in the cool wake of a moving hurricane, *J. Geophys. Res.*, *113*, C07010, doi:10.1029/2007JC004393.

Reid, J. S., E. M. Prins, D. L. Westphal, C. C. Schmidt, K. A. Richardson, S. A. Christopher, T. F. Eck, E. A. Reid, C. A. Curtis, and J. P. Hoffman (2004), Real-time monitoring of South American smoke particle emissions and transport using a coupled remote sensing/box-model approach, *Geophys. Res. Lett.*, *31*, L06107 doi:10.1029/2003GL018845.

Reid, J. S., E. J. Hyer, E. M. Prins, D. L. Westphal, J. Zhang, J. Wang, S. A. Christopher, C. A. Curtis, C. C. Schmidt, and D. P. Eleuterio (2009), Global monitoring and forecasting of biomass-burning smoke: Description of and lessons from the Fire Locating And Modeling of Burning Emissions (FLAMBE) program, *IEEE J. Sel. Topics Appl. Earth Observ.*, *2*, 144–162.

Remer, L. A., Y. Kaufman, D. Tanré, S. Mattoo, D. Chu, J. V. Martins, R. R. Li, C. Ichoku, R. Levy, and R. Kleidman (2005), The MODIS aerosol algorithm, products, and validation, *J. Atmos. Sci.*, *62*, 947–973.

Roberts, G. J., and M. J. Wooster (2008), Fire detection and fire characterization over Africa using Meteosat SEVIRI, *IEEE Trans. Geosci. Remote Sens.*, *46*, 1200–1218.

Roberts, G., M. J. Wooster, and E. Lagoudakis (2009), Annual and diurnal African biomass burning temporal dynamics, *Biogeosciences*, *6*, 849–866, doi:10.5194/bg-6-849-2009.

Roberts, G. J., M. J. Wooster, G. L. W. Perry, N. Drake, L. M. Rebelo, and F. Dipotso (2005), Retrieval of biomass combustion rates and totals from fire radiative power observations: Application to southern Africa using geostationary SEVIRI imagery, *J. Geophys. Res.*, *110*, D21111, doi:10.1029/2005JD006018.

Schell, B., I. Ackermann, H. Hass, F. Binkowski, and A. Ebel (2001), Modeling the formation of secondary organic aerosol within a comprehensive air quality model system, *J. Geophys. Res.*, *106*, 28,275–28,293.

Seiler, W., and P. Crutzen (1980), Estimates of gross and net fluxes of carbon between the biosphere and the atmosphere from biomass burning, *Clim. Change*, *2*(3), 207–247.

Shi, Y., J. Zhang, J. S. Reid, E. J. Hyer, and N. C. Hsu (2013), Critical evaluation of the MODIS Deep Blue aerosol optical depth product for data assimilation over North Africa, *Atmos. Meas. Tech.*, *6*, 949–969, doi:10.5194/amt-6-949-2013.

Smirnov, A., B. N. Holben, T. F. Eck, O. Dubovik, and I. Slutsker (2000), Cloud-screening and quality control algorithms for the AERONET database, *Remote Sens. Environ.*, *73*(3), 337–349.

Stockwell, W., P. Middleton, J. Chang, and X. Tang (1990), The second generation regional acid deposition model chemical mechanism for regional air quality modeling, *J. Geophys. Res.*, *95*, 16,343–16,367.

Tesche, M., A. Ansmann, D. Müller, D. Althausen, R. Engelmann, V. Freudenthaler, and S. Groβ (2009), Vertically resolved separation of dust and smoke over Cape Verde using multiwavelength Raman and polarization lidars during Saharan Mineral Dust Experiment 2008, *J. Geophys. Res.*, *114*, D13202, doi:10.1029/2009JD011862.

The NCAR Command Language (Version 6.1.2) [Software] (2013), Boulder, Colorado: UCAR/NCAR/CISL/VETS, doi:10.5065/D6WD3XH5.

Tucker, J. C., and E. S. Nicholson (1999), Variations in the size of the Sahara Desert from 1980 to 1997, *Ambio*, *28*, 587–591.

Wang, J., S. Christopher, U. Nair, J. Reid, E. Prins, J. Szykman, and J. Hand (2006), Mesoscale modeling of Central American smoke transport to the United States: 1."Top-down" assessment of emission strength and diurnal variation impacts, *J. Geophys. Res.*, *111*, D05S17, doi:10.1029/2005JD006416.

Wang, J., C. Ge, Z. Yang, E. J. Hyer, J. S. Reid, B. N. Chew, M. Mahmud, Y. Zhang, and M. Zhang (2013), Mesoscale modeling of smoke transport over the Southeast Asian Maritime Continent: Interplay of sea breeze, trade wind, typhoon, and topography, *Atmos. Res.*, *122*, 486–503.

Winker, D. M., M. A. Vaughan, A. Omar, Y. Hu, K. A. Powell, Z. Liu, W. H. Hunt, and S. A. Young (2009), Overview of the CALIPSO mission and CALIOP data processing algorithms, *J. Atmos. Oceanic Technol.*, *26*, 2310–2323.

Zhang, X., S. Kondragunta, J. Ram, C. Schmidt, and H. C. Huang (2012), Near-real-time global biomass burning emissions product from geostationary satellite constellation, *J. Geophys. Res.*, *117*, D14201, doi:10.1029/2012JD017459.

Zhao, C., X. Liu, L. Leung, B. Johnson, S. McFarlane, W. Gustafson Jr., J. Fast, and R. Easter (2010), The spatial distribution of mineral dust and its shortwave radiative forcing over North Africa: Modeling sensitivities to dust emissions and aerosol size treatments, *Atmos. Chem. Phys.*, *10*, 8821–8838.